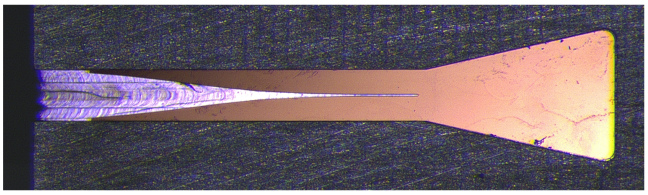

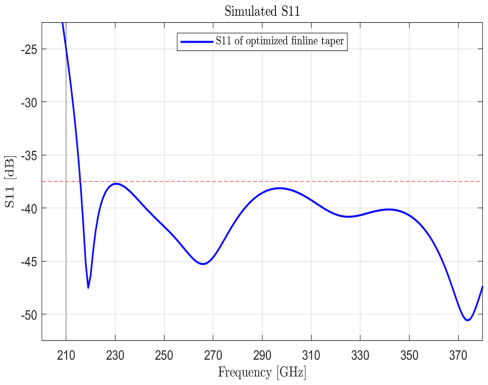

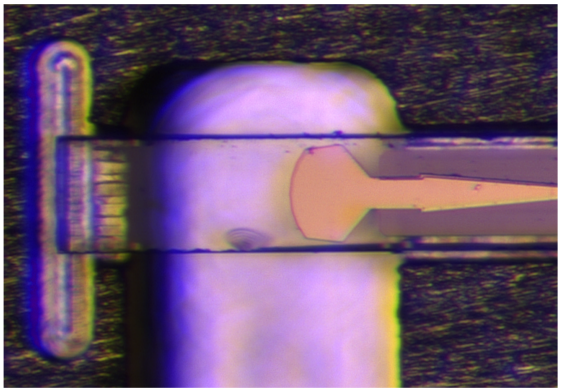

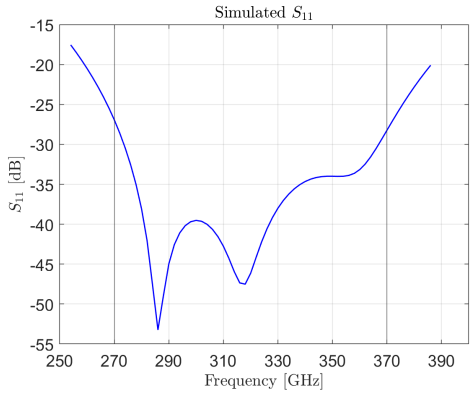

Design, fabrication and characterization of wideband terahertz waveguide terminations

Master's thesis in Wireless, Photonics and Space engineering

Karl Birkir Flosason

Department of Space, Earth and the Environment
CHALMERS UNIVERSITY OF TECHNOLOGY
Gothenburg, Sweden 2023
www.chalmers.se

Master's thesis 2023

Design, fabrication and characterization of wideband waveguide terminations

Karl Birkir Flosason

CHALMERS
UNIVERSITY OF TECHNOLOGY

Department of Space, Earth and the Environment
Onsala Space Observatory
Group for Advanced Receiver Development - GARD
Chalmers University of Technology
Gothenburg, Sweden 2023

Design, fabrication and characterization of wideband waveguide terminations

Supervisor: Professor Vincent Desmaris, GARD
Examiner: Professor Victor Belitsky, GARD

Group for Advanced Receiver Development (GARD)
Department of Space, Earth and the Environment
Division of Onsala Space Observatory
Chalmers University of Technology
SE-412 96 Gothenburg
Telephone +46 31 772 1000

Cover: Microscope pictures and simulated S_{11} of the waveguide terminations
Printed by Kompendiet AB, Göteborg. Gothenburg, Sweden 2023

Design, fabrication and characterization of wideband waveguide terminations

Karl Birkir Flosason
GARD
Onsala Space Observatory
Department of Space, Earth and the Environment
Chalmers University of Technology

Abstract

This thesis reports on two novel designs for high performance, wideband waveguide terminations for terahertz frequencies, demonstrated here in the range 210-370 GHz corresponding to ALMA bands 6-7.

With advancing technology in the design and fabrication of high sensitivity radioastronomy receivers, each component and aspect of the system needs to be pushed to the limits when it comes to performance and bandwidth. The highest sensitivity and state-of-the-art receivers today for radioastronomy use 2SB mixer topologies, which require terminations to terminate the fourth port of a waveguide RF hybrid coupler. Reflections from that termination will both increase the level of noise generally but also risk introducing spectral line images or ghosts from the heterodyne downmixing process, which may cause confusion of spectral lines when the tools are used for spectroscopy. Minimizing the reflections from that waveguide termination is a step in improving over-all performance, and taking full advantage of increased performance of the 2SB topology.

The goal of the project was to design, fabricate and measure two distinct and novel termination designs, fabricated with well established methods, and materials with known and reliable behaviours in cryogenic operation, and achieve the best possible performance over the widest possible bandwidth. One design based on an E-probe on quartz substrate, showing in simulations S_{11} < -26 dB over 270-370 GHz, and another design based on a tapered finline structure showing in simulations S_{11} < -37.5 dB over 220-390 GHz. Both designs use TiN resistive thin-film to dissipate the RF energy in ohmic losses.

To validate and verify the design and fabrication process, the performance was then measured using a VNA and the required frequency extensions. Measuring reflection accurately at such low levels and at these frequencies is challenging, and the measurements are likely to underestimate the real performance. Uncertainties in the measurements are described and their scale evaluated both by measurements and simulation.

Keywords: Terahertz, waveguide termination, wideband, rf load, waveguide load, VNA, microwave metrology, reflection coefficient.

Acknowledgements

First and foremost I would like to extend my gratitude to my examiner Victor Belitsky for attentively overseeing this work, being generous with his time and wealth of knowledge.
I would like to thank my supervisor Vincent Desmaris for having me in on this project, and his helpfulness and patience in guiding the process.
Huge thanks to Denis Meledin for his incredible patience with extensive staring through the microscope and delicately mounting ludicrously small objects to unbelievable precision, and help with the measurements.
Thanks to Sven-Erik Ferm for this considerable skill with the machining, and attention to detail, which is indispensable in fabricating waveguide blocks to such high quality, as this project shows beyond doubt. Thanks to Leif Helldner for the excellent waveguide block layout and struggling through strange file import/export problems with me, and help with the measurements. Thanks for Alexey Pavolotskiy for saving us with mask printing, and being there for good advice. And last but not least thanks to Cristian Daniel López for his appreciated insights, useful discussions, simulation advice, company and help in the clean room.

This project would not have been possible, and not as fun, without the great team at GARD.

It has been a pleasure and an honor, and the highlight of my time in Chalmers to take part in this work.

In loving memory of my father, dr. Flosi Karlsson TF3FX (1960-2013),
whose key is now silent.

Karl Birkir Flosason, Gothenburg, June 2023

List of Acronyms

Below is the list of acronyms that have been used throughout this thesis listed in alphabetical order:

2SB	Two-sidebands, sideband separating
AC	Alternating Current
ALMA	Atacama Large Millimeter/submillimeter Array
CAD	Computer-Assisted Drawing
DC	Direct Current
FBW	Fractional Bandwidth
FIR	Far-infrared
GHz	Gigahertz (10^9 Hz)
IF	intermediate frequency
IR	Infrared
LO	Local Oscillator
MMIC	Monolithic Microwave Integrated Circuit
RF	Radio frequency
RFI	Radio Frequency Interference
SIS	Superconductor-Insulator-Superconductor
SSR	Sideband-Separation Ratio
THz	Terahertz (10^{12} Hz)
VNA	Vector Network Analyzer

Physical constants

c	$= 1/\sqrt{\mu_0 \varepsilon_0} = 299792458$	m/s	Speed of light in vacuum
η	$= \sqrt{\mu_0/\varepsilon_0} \approx 376.73$	Ω	Wave impedance of free space
μ_0	$= 4\pi \times 10^{-7}$	H/m	Magnetic permeability of free space
ε_0	$\approx 8.8541878128 \times 10^{-12}$	F/m	Electric permittivity of free space

Contents

List of Figures

List of Tables

1

Preface

In the autumn of 1609 in the town of Padua in Italy, Galileo Galilei pointed his newly built telescope at the moon. Through the magnifying lenses he could clearly see the rough, cratered and uneven surface of the moon, which was in stark contradiction to the dominant cosmology of his time. According to that Aristotelian worldview, the heavens were perfect and immutable, and the moon should be a smooth, ideal sphere. Soon after, with an improved telescope, he turned to the planets and saw that they looked different from the point-like stars, and discovered that Jupiter had moons. He also observed that Venus shows full phases through its orbit, which did not fit with the old Ptolemic, earth-centric model of the solar system, but confirmed the Copernican helio-centric model, which was still a serious debate then. This new instrument shattered the old view of the world, and heralded a new age of observational astronomy. An age of basing our understanding of the cosmos on empirical data acquired by observations through ever improving instruments.

Familiarity with the night sky had been useful through human history. The phases of the moon, the equinoxes and solstices, and the rise and fall of star constellations keep track of time and the changing of the seasons. The Pole Star guides travellers by indicating cardinal north. But when we started fully applying our advancing tool culture to observing it, fundamental changes to our view of the world and our place in it followed. Johannes Kepler derived the laws of planetary motions, based on detailed observations of their orbits made by Tycho Brahe. This would serve as a foundation and inspiration for Newton's theory of gravitation. Since then, by more meticulous collection of data with ever improving instruments, much of our fundamental understanding of the universe and our place in it has been revolutionized, and a more accurate one reestablished more firmly

Experiments with radio receivers in the early and mid- 20th century revealed that outer space was the source of a great deal of radio signals. Telescopes for radiowaves were developed to explore that, and they revealed that scientific discoveries in space were in no way limited to visible light and optical telescopes, but the whole electromagnetic spectrum conveys to us evidence of a great range of processes and phenomena in space, many of which are otherwise undetectable.

Through these tools we have discovered and mapped the Cosmic Microwave Background, and learned from it about the origin, composition and structure of the universe. Deviations from the expected behaviour of gravity on large scales has been found in the rotations of galaxies. We have confirmed the widespread existence of water and even complex organic molecules in distant celestial objects, witnessed the formations of solar systems and the heat glow of accretion discs around swirling black holes.

What more is out there yet to be discovered, is unknown. But as we build and deploy even better instruments, we will find out.

2
Introduction

With wavelengths in the range of 1-0.03 mm, the terahertz range of approximately 0.3-10 THz sits between infrared light and microwaves in the electromagnetic spectrum. It has until recent years been the most underutilized part of the electromagnetic spectrum. With advances in detector technology and sources suitable for use as oscillators, science has increasingly been taking advantage of this range of frequencies. Photon energies at those frequencies are relatively low so the radiation is harmless to humans and other organisms, but with shorter wavelengths than microwaves, the achievable angular resolution is greatly enhanced. Additionally, a wide variety of molecules have uniquely identifiable emission spectra in this frequency range, making it very useful for spectroscopic identification and analysis of chemical compositions [1]. In astronomy, THz instruments have proven to be a powerful part of the toolkit, and given us eyes to see parts of our universe that are otherwise invisible to us.

Among the largest and most ambitious projects in ground-based astronomy is the radiotelescope ALMA (Atacama Large Millimeter/submillimeter Array) [2]. Located in the high plateau of the Atacama desert in Chile, ALMA consists of 66 individual antennas, operating together as an interferometer with adjustable baselines from 150 meters to 16 kilometers. Each ALMA antenna has 10 different receivers to cover different parts of the frequency range between 35 and 950 GHz, each receiver built by different teams in an international co-operative effort. The research group GARD, Group for Advanced Receiver Development, in Chalmers, has to date contributed to developing and fabricating receivers for two of the bands, band 2 and 5, as a part of the Onsala Space Observatory group, OSO [2].

2.1 Motivation

The signals received in most fields of radioastronomy are of extremely low power, so the highest achievable sensitivity in receiver technology is sought after and the tools constantly developed toward that goal. Since they are also intended for high frequency-resolution spectroscopy to identify molecules, it is important that spectral lines are not superimposed such as by image effects in the heterodyne frequency conversion process, which could cause spectral line confusion. One way to achieve both these goals is the 2SB or sideband separating receiver topology, which separates the sidebands using a mixer layout such as shown in Fig. 2.1, or Superconductor-Insulator-Superconductor, mixing technology. This setup also further reduces the effects of atmospheric noise in the reception [3], and the SIS mixer approaches the

quantum limit of noise performance.
Receivers based on this principle have shown very good performance, such as in the recent SEPIA instrument for the APEX telescope [4] and ALMA band 5 [5]. But this improved performance is dependent on how effective the sideband separation is, as characterized by the figure-of-merit Sideband Separation Ratio (SSR). A system analysis by [6] shows how improving the SSR from its current state-of-the-art value of around 10 dB up to 20 dB would significantly improve over-all performance, reduce integration time and all but eliminate spectral line confusion. That analysis points to three of the main components of current systems that affect this figure: reflections off the SIS mixer itself, isolation between ports of the RF hybrids, and reflections from the RF load. Improved SSR will lower system noise, which reduces required observation time, and will reduce effects of unwanted artefacts such as image superposition on the signal, which may confuse spectral lines in spectroscopy [7]. RF loads with lower reflections will be one of the improvements needed to reduce internal reflections in the receiver assembly and thus improve the SSR of 2SB SIS receivers.

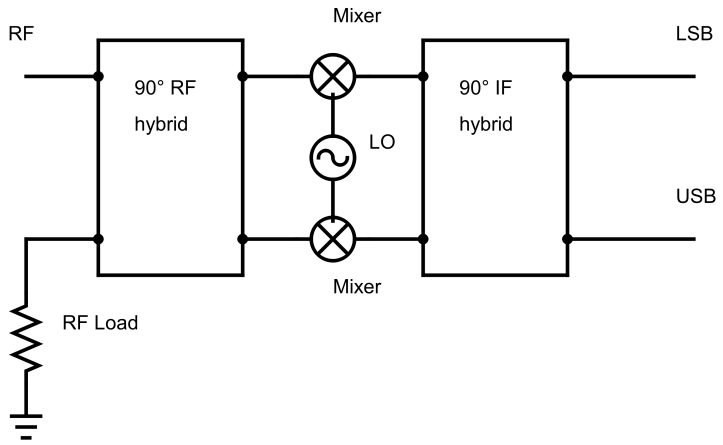

Figure 2.1: A block-schematic view a 2SB mixer setup, showing the placement of the RF load on one port of the 90° RF hybrid

Matched RF loads have the function of maximally absorbing RF energy with minimal reflections, such as at the termination of transmission lines or waveguides. They are a standard component and various commercially available solutions exist at those frequency ranges which are in common use. Matched loads with very low reflections are used in measurement systems, and terminations with high power dissipation can be used as dummy loads in power measurements or dry-runs of power amplifier setups. They are also necessary parts of system components where one output port needs to be terminated, such as some couplers and RF hybrids, as reflections would otherwise reflect back into the system and cause interference or increase the noise level, or in the characterization and measurements of multi-port devices where the parameters will not be correctly measured unless the unused ports are terminated with a matching load. Imperfect terminations, ones that are not matched or in other ways do not absorb well enough, cause reflections resulting

in standing waves and interferences and more noise in the system. In radioastronomy receivers in particular, reflections from imperfect loads increase noise in the system and can introduce false signals such as spectral line confusion.

Designing and fabricating a wideband, high performance waveguide termination at millimeter and sub-millimeter wavelengths will require high-precision manufacturing methods. But it will be favorable if the fabrication method is kept relatively simple and not with excessively tight manufacturing tolerances or with materials that are hard to work with. Components for such short wavelengths are generally inherently small, so in some cases larger components are well acceptable and may even facilitate an easy installation.

2.2 Prior work

A typical way of implementing a matched load as a waveguide termination is by way of a lossy conductor or a lossy dielectric as an absorber, or combining both together. Several RF loads proposed for use in THz radioastronomy receivers and other RF systems utilize a commercially available epoxy-based material loaded with fragments of a lossy conductor [8]. This material has been characterized over a large frequency range at temperatures of both 300 K and 5 K by [9] and by [10]. Generally it is shaped into tapering cones or wedges and placed in the end of a waveguide, see [11] and [12]. Other approaches have been explored as well for these frequency ranges, such as using a linear tapered finline of thick, lossy silicon shaped by etching, inserted in the waveguide [13], or an elliptically-shaped resistive thin-film on substrate [14]. A matched load as a hidden fourth-port in a waveguide power splitter/combiner T-junction designed and demonstrated by Gouda et al. [15] could be implemented for this functionality.

At millimeter wave frequencies it becomes more challenging to implement a good RF load. Methods developed for lower frequencies become less effective. Parasitic inductances and capacitances in conventional resistors present high reactance at those high frequencies, which limits or entirely prevents power transfer and absorption. Methods from higher frequencies, visible light, infrared (IR) or far-infrared (FIR), are not viable either. Since materials that present as opaque to IR and FIR become increasingly transparent at THz frequencies, all known black, matte paints and opaque materials are not effective [16], as their thickness is diminishing compared to the skindepth at the frequencies in question.

While some of these approaches have produced useful terminations, different materials and fabrication methods allowing finer control of the shape to achieve a better impedance match and absorption could push the performance into the levels required for the next generation of radioastronomical instruments, where performance of each system component is crucial.

3

Theory

This section introduces the theory as it relates to the design process and its results, following established literature in the field, such as Pozar [17] and other textbooks as is relevant, such as [18] [19] [20]. This involves the main building elements such as transmission lines, their most relevant parameters and the formulas to calculate them, as fits within the scope of this work.

3.1 Resistivity at high frequencies, and skin depth

Following Ohm's law, resistance is the ratio between current and the voltage that is required to make it flow, $R = V/I$, or equivalently, the energy lost by electrons moving through an imperfect conductor. Resistance is a function of the material property bulk resistivity ρ, and the physical dimensions of the conductor, or that is, its cross-sectional area $A = w \cdot t$ and length L. A practical parameter for thin-films is sheet resistance, $\rho/t = R_\square$, or resistance-per-square, and $R_\square \frac{L}{w} = R$, or more comprehensively:

$$R\ [\Omega] = \rho \frac{L}{w \cdot t} = R_\square \frac{L}{w} \tag{3.1}$$

The resistivity of conductors increases proportionally with frequency, as $\sqrt{f}$, if the thickness is greater than the skindepth. This is due to eddy currents inside the bulk of the conductor, caused by the rapidly changing electromagnetic fields, which oppose the flow of current, causing the current density to concentrate by the conductors' surface rather than having a more even distribution over the conductors cross-section as it does at DC. The current density decays exponentially from the surface and into the conductor. This is called the skin effect, and the skin depth, δ_s, is defined as the distance at which the fields inside the metal have been reduced to $1/e$ of their value at the surface. The skin depth for a given conductor and frequency can be calculated as:

$$\delta_s = \sqrt{\frac{2}{\sigma \omega \mu}} \tag{3.2}$$

Where $\omega = 2\pi f$ is the angular frequency, $\mu = \mu_0 \mu_r$ is magnetic permeability and $\sigma = 1/\rho$ is the material bulk conductivity. This applies under the approximation that the mean free path of an electron is much shorter than the skindepth, as noticed by Heinz London [21]. It also assumes a smooth conductor surface, which is not necessarily the case, and a rougher surface results in a longer conduction path along

the surface, which effectively increases the resistance. At cryogenic temperatures, the resistivity of normal conductors increases even more with high frequencies, by the anomalous skin effect [22, 23, 24]. This exponential decay of current density in the bulk metal yields rapidly diminishing returns of increased conductivity from increasing the thickness of a conductor. Skin depths can also be used in plural form, referring to the depth at which current density has been reduced by factor $1/e^N$, after N skindepths from the conductors' surface. As a rule of thumb it is sometimes considered enough to use 3 or 4 skin depths of thickness, which reduces the conductivity by only $1/e^3 \approx 0.05$ or $1/e^4 \approx 0.02$, to maintain conductivity as good as it gets without inefficient use of materials.
The lowest sheet resistance achievable for a given frequency and bulk conductivity can be calculated as:

$$R_{\square,RF,min} = \sqrt{\frac{\omega\mu}{2\sigma}} \tag{3.3}$$

If the thickness of the conductor is much thinner than the skindepth, i.e. $t << \delta_s$, its resistance is dominated by its thinness rather than the skin effect, so its sheet resistance at high frequency approaches its sheet resistance at DC.

3.2 Thin film resistors

Resistive thin films are used for some applications in microwave circuits, here it is used as a termination to dissipate RF energy. They can be made with various metal alloys such as Tantalum Nitride (TaN) or Nickel-Chromium (NiCr) [25], but here it is implemented with a Titanium-Nitride [26]. The resistivity is controlled by the amount of Nitrogen, and can then be manufactured to the desired sheet resistance by controlling the thickness of the film, although the available range of adjustment there is limited by the manufacturing process. To then achieve a target resistance value, the ratio between width and length is adjusted, following the formulas 3.1. Thin-film resistors at RF have been characterized by [27] and [28] among others.

3.3 Transmission lines and waveguides

As frequency increases, the length of conductors risks becoming a significant proportion of the length of the wave, λ. The voltage in different locations on a conductor can no longer be assumed to be the same throughout as in classical circuit theory, as it follows the transmitted wave. To handle these cases a new circuit theory needs to be developed, taking the characteristics and dimensions of the transmission lines fully into account as they relate to the propagation of the electric and magnetic fields, and the power they transfer.

3.3.1 General transmission line characteristics

Modelling the transmission line as sequence of multiple small segments, where each segment can be modelled as resistors and inductors in series, and resistors and

capacitors in parallel, its characteristic impedance Z_c, can be calculated as:

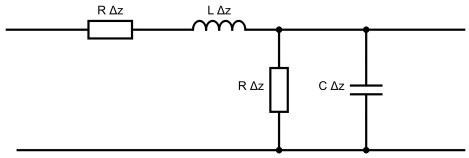

$$Z_c = \sqrt{\frac{R + j\omega L}{G + j\omega C}} \tag{3.4}$$

Where the R is the resistance, G is shunt conductance, and L and C are inductance and capacitance, per unit length. The Δz indicates that all the values are per small segment. The impedance is generally a complex number, a real valued resistance and imaginary reactance, $Z_L = R_L + X_L$. A transmission line would sometimes be approximated as lossless and with no shunt conductance, setting $R = 0$ and $G = 0$, reducing the characteristic impedance to $Z = \sqrt{\frac{L}{C}}$, which is a pure real number.

Another important parameter for transmission lines is the propagation constant γ:

$$\gamma = \alpha + j\beta = \sqrt{(R + j\omega L)(G + j\omega C)} \tag{3.5}$$

Where α is its attenuation factor and β the wavenumber. The propagation constant describes how the phase and magnitude of a wave travelling on the transmission line get translated forward, or with l as distance or location on the line:

$$V = V^+ e^{-\gamma l} + V^- e^{\gamma l} \tag{3.6}$$

In the exponent, a real-valued $\alpha \neq 0$ results in an exponential decay of the voltage in the positive direction, and the imaginary-valued β a periodic voltage wave.

For a line with $R = 0$ and $G = 0$ and thus no loss, the the attenuation is taken to be 0, or $\alpha \approx 0$. The attenuation factor α is the sum of different factors that all contribute to attenuation, i.e. $\alpha = \alpha_c + \alpha_d + \alpha_r + \ldots$, where the subscripts denote conductor, dielectric and radiative and other possible losses. Conductor losses, or ohmic losses are due to current flowing through an imperfect conductor and relate to the resistance and the impedance, and for low losses can be roughly approximated as:

$$\alpha_c \approx \frac{2R}{Z_0} \tag{3.7}$$

Combining the aforementioned elements of transmission lines, the telegrapher's equation expresses what impedance a transmission line presents at its inputs,Z_{in}, given its own characteristic impedance Z_c according to formula 3.4, the terminating impedance Z_L, it's propagation constant γ and its length l.

$$Z_{in} = Z_0 \frac{Z_L + Z_0 \tanh(\gamma l)}{Z_0 + Z_L \tanh(\gamma l)} \tag{3.8}$$

The goal of a transmission line is to deliver power, from a source to a load. How well it does this depends on the match or mismatch of the source, transmission line and load. A well matched sequence delivers power much better, and over a wider frequency range than a badly matched one, as expressed in the following formula.

$$P_R = \frac{|V_L|^2}{8R_L}\frac{4R_S R_L}{|Z_S + Z_L|^2} = \frac{|V_L|^2}{8R_L}(1 - |\Gamma_{load}|^2) \tag{3.9}$$

Where V_L is the voltage across the load, and R_S and R_L is the internal resistance to the source, and the load resistance respectively. Maximum power transfer between a source and a load is achieved if their impedances are conjugate matched, $Z_{source} = Z^*_{load}$. But for maximal bandwidth both components should have purely real impedance or as close to purely real as possible, since any imaginary component to the impedances of each will in the general case not stay perfectly conjugate over a wide range of frequencies and would thus limit the bandwidth of this match and thus the power transfer. The implication of this for a waveguide termination is that it needs to present an impedance as close to real as possible.

3.3.2 Scattering parameters, S-matrix

A useful way of measuring and describing microwave systems and components is in terms of power of travelling waves, either reflected or incident [20]. When devices have multiple inputs and outputs, the relations are conveniently presented in a so-called scattering parameters, the S matrix, shown for an n-port device:

$$\mathbf{S} = \begin{bmatrix} S_{11} & \dots & S_{1n} \\ \vdots & \ddots & \vdots \\ S_{n1} & \dots & S_{nn} \end{bmatrix} \tag{3.10}$$

Which translates between incident and reflected voltage waves between the ports in the following way:

$$[V^-] = [S][V^+] \tag{3.11}$$

And each entry of the S matrix can be expressed as

$$S_{ij} = \left.\frac{V_i^-}{V_j^+}\right|_{V_k^+ = 0 \text{ for } k \neq j} \tag{3.12}$$

Or stating the same in plain words, following the theory outlined in Pozar [17]: If you drive port j with an incident wave of voltage V_j^+, and then measure the amplitude of the reflected wave at port i, V_i^+, while any other ports are terminated with a matching load, their ratio is the S parameter S_{ij}. Keeping in mind that $i = j$ is allowed, and presents how much is reflected back to the same port.

The S-parameters then relate the incident and reflected waves a and b in the following way, as shown in the following figure.

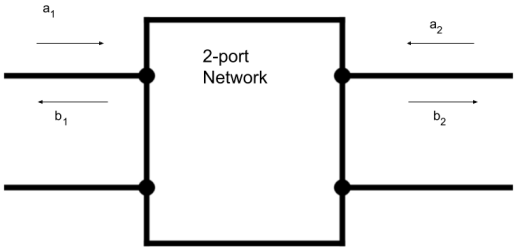

$$b_1 = S_{11}a_1 + S_{12}a_2$$
$$b_2 = S_{21}a_1 + S_{22}a_2 \tag{3.13}$$

Figure 3.1: Incident and reflected waves, a and b, in a 2-port network

The most important S-parameter in this work is the S_{11}, as it relates to the reflection coming back out of port 1 when it is excited with a wave, and is thus the obvious measure of the performance of a waveguide termination. For one-port, S_{11} is equivalent to its reflection coefficient, Γ, and a lower value means a lower reflection.

3.3.3 Chain scattering parameters, T-matrix

Another note-keeping and calculation method for multi-port networks in microwave systems is the T-matrix, or chain scattering matrix. Different from the S-matrix, the T-matrices of cascaded microwave devices can be cascaded themselves, to calculate the total T-matrix of the chain. This can be a useful tool, such as for de-embedding fixtures for VNA measurements. The 2x2 T-matrix is related to the 2x2 S-matrix in the following way:

$$\mathbf{T} = \begin{bmatrix} T_{11} & T_{12} \\ T_{21} & T_{22} \end{bmatrix} = \begin{bmatrix} S_{21}^{-1} & -S_{21}^{-1}S_{22} \\ S_{21}^{-1}S_{11} & S_{12} - S_{11}S_{21}^{-1}S_{22} \end{bmatrix} \tag{3.14}$$

Since the T-matrices are invertible, if a measured device-under-test (DUT) is embedded in a test fixture with known S- or T-parameters:

$$[T_{measured}] = [T_A][T_{DUT}][T_B] \tag{3.15}$$

Its de-embedded T-matrix can be found simply using matrix algebra

$$[T_{DUT}] = [T_A]^{-1}[T_{measured}][T_B]^{-1} \tag{3.16}$$

Which is then trivial to convert back to the S-matrix.

3.3.4 Microstrip line

Microstrip lines consist of a conductor separated from a conducting ground plane by a dielectric. They have become ubiquitous in electric circuits for several reasons, such as ease of manufacture and system integration, as they make for convenient integration with other circuit elements such as mixers, filters and amplifiers. Since microstrip lines have two conductors, they can support a TEM mode of propagation, but other modes may arise. At the TEM mode, the impedance of an ideal microstrip line is nearly independent of frequency.

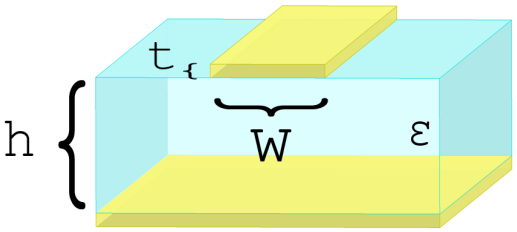

Figure 3.2: Section of microstrip line, with the conductor and ground plane in yellow and dielectric as transparent blue

The impedance of a microstrip line depends on the width of the conductor, w, the separation distance from the ground plane, d, and the permittivity of the dielectric ε. Formulas to calculate their impedance have been developed from empirical methods, based on curve-fitting to measurements [17].

$$Z_0 = \begin{cases} \frac{60}{\sqrt{\varepsilon_r}} \ln\left(\frac{8h}{W} + \frac{W}{4h}\right) & \begin{cases} W/h \leq 1 \end{cases} \\ 120\pi / \sqrt{\varepsilon_e}[W/h + 1.393 + 0.667 \ln(W/h + 1.444)] & \begin{cases} W/h \geq 1 \end{cases} \end{cases} \tag{3.17}$$

Where ε_e is the effective relative permittivity

$$\varepsilon_e = \frac{\varepsilon_r + 1}{2} + \frac{\varepsilon_r - 1}{2} \frac{1}{\sqrt{1 + 12h/w}} \tag{3.18}$$

When designing with microstrip lines, they are often first approximated as lossless, this makes its impedance purely real valued. In the design presented in later chapters the microstrip line is deliberately made of a lossy, resistive material, as it is used as an absorber. This adds series capacitance to its impedance, as characterized by [27], and can be seen from formula 3.4 for transmission line impedance.

These formulas approximate a microstrip where the electric field only interacts between the microstrip and the ground conductor. Microstrips are often enclosed in conductive boxes, and here in a substrate channel described in 4.1.2, which will affect the distribution of the electric field, and thus the effective permittivity, which affects the characteristic impedance. These formulas may still serve as initial approximations, but more accurate values need to be found as needed using full-wave EM simulators [19].

3.3.5 Slotline

The slotline is implemented as two metal strips separated by a gap, on top of a dielectric material substrate. Like the microstrip line, the electric field is partially in air and partially in the dielectric substrate, but for the slotline the electric field concentrates in the gap between the conductors. The slotline has the benefit of not requiring a ground plane under the substrate, but the drawback that it demonstrates high losses. The defining attributes for the impedance are the width of the separating gap, the height of the substrate and its dielectric permittivity.

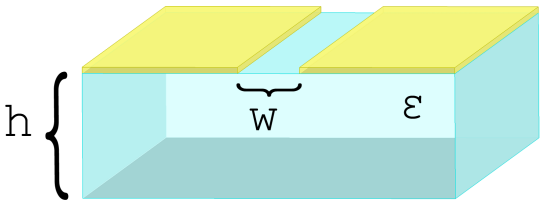

Figure 3.3: Section of slotline on substrate

Similarly to the microstrip line, the impedance of slotlines has been explored by measurements and curvefitting, as described in [18], although limited to proportions $0.02 \leq W/h \leq 1$, or that is, with a gap W not wider than the substrate thickness h.

3.3.6 Waveguide

A waveguide consists of a conductive or reflective boundary surrounding a dielectric. This is most commonly implemented as an air-filled rectangular metal pipe. Waveguides see widespread use in RF systems for their relative ease of manufacture and low attenuation at high frequencies, and shielding from radio interference. Since high frequency radioastronomy systems generally use a parabolic reflector to collect and focus the incoming radiowaves, the highest coupling factor into a RF front-end system is achieved with a corrugated horn on waveguide.

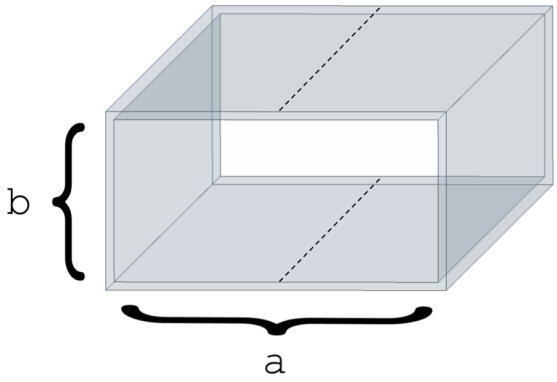

Figure 3.4: Section of rectangular waveguide of width a, and standard proportions $b = a/2$. Also showing in dashed lines, the centerline of dimension a, along which the waveguide can be split.

The waveguide only uses a single conductor, therefore it doesn't support a TEM propagation mode, only TM and TE modes. The impedance of a waveguide is not uniquely defined, but a common definition is the wave impedance of the mode being used, here Z_{TE} :

$$Z_{TE} = \frac{k\eta}{\beta}, \quad \beta = \sqrt{k^2 - k_c^2} \tag{3.19}$$

$$k = \omega\sqrt{\mu\varepsilon}, \quad k_c = \sqrt{\left(\frac{m\pi}{a}\right)^2 + \left(\frac{n\pi}{b}\right)^2} \tag{3.20}$$

Where m and n are integers corresponding to the different modes of field distribution, and a and b are the waveguide dimensions. Inconveniently, the impedance of waveguides is not constant over frequency, but is much higher on the lower end of its band, but for the standard proportions $a/b = 2$ its Z_{TE} impedance converges to 400 ohms as the frequency increases. The mode waveguides are generally designed to use is the lowest TE mode ofTE_{10}, but for any TE_{mn} mode the cut-off frequency can be found as:

$$f_c = \frac{c}{2\pi\sqrt{\varepsilon_r}}\sqrt{\left(\frac{m\pi}{a}\right)^2 + \left(\frac{n\pi}{b}\right)^2} \tag{3.21}$$

For waves propagating in the fundamental mode, TE_{10}, virtually no currents flows across the centerline shown in figure 3.4. This enables manufacturing methods such as producing the waveguide in two halves, a splitblock, split along the middle of "a", or using those sides for inputs and outputs into the waveguide, which will be utilized in the designs presented in the upcoming sections.

3.3.7 Finlines

The finline was proposed by Meier [29] and found to be very useful at high frequencies, several standard components for millimeter frequencies were subsequently developed based on that technique [30], such as matching networks, filters, directional couplers and antennas [31] and waveguide-to-substrate transitions [32]. Several variations of the finline concept exist, but the one used here consists of a thin, metallized, dielectric slab or substrate, inserted parallel to the E-field, and along the propagation axis of a waveguide. The slabs come out of the wider sidewalls and towards the center, but remain separated by a gap of variable width. The gap width, substrate thickness and permittivity are the defining features of the finline, having the greatest impact on its impedance. Impedance decreases with a narrower gap for a given substrate.

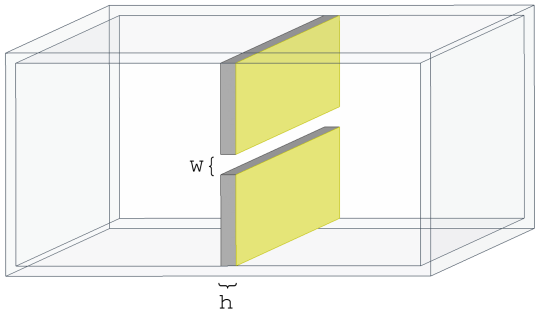

Figure 3.5: Small segment of finline in waveguide. Substrate shown in gray, conductor in yellow, surrounding waveguide made transparent

Approximate formulas exist for the impedance and guided wavelengths, but thin and high permittivity dielectric with a separation width large compared to the substrate thickness. The formulas are too elaborate and long to be presented here, but they are described in more detail in [18] among other literature [29], [30], [31].

The substrate is inserted into a waveguide, the electric field concentrates in the gap between the conductors.

Various approaches at synthesizing smooth finline tapers have been published, such as [31] and [33].

3.4 Waveguide-to-substrate transitions

Waveguides are commonly used at the front-end of radiosystems at very high frequencies, but the components that work with the signal are on substrates, such as mixers and transistors, so the need arises to interface or transition between those two propagating media. It is important that this transition couples effectively with the waveguide and captures as much of the RF energy as possible.

Several designs have been proposed to achieve this, two categories of which will be mentioned here. One approach is to use a conductor on a suspended substrate as a probe inserted parallel into the electric field, a so-called E-probe, such as the radial probe by Kooi et. al. [34] in a full-height waveguide, or at higher frequencies by [35], or the one developed by Gouda et. al. [15] for use in a power-divider/combiner. Others have suggested dipoles [36] or butterfly shapes [37]. Another category is to use a finline structure such as proposed by [29], and has been shown by [32] to be very effective and broadband as an interface between waveguide and SIS mixer.

3.5 Impedance matching, multi-section transformers and tapers

With impedance playing a central role in the design and function of microwave systems, transforming it to achieve a match between different systems or propagating mediums is crucial.

The quality of matching between source impedance Z_0 and load impedance Z_L can be expressed with the number $\Gamma = \frac{Z_0 - Z_L}{Z_0 + Z_L}$, which is optimized at $\Gamma = 0$ when $Z_0 = Z_L$. A multi-section transformer is based on inserting several transmission line sections in a sequence of impedances in the range between Z_0 and Z_L, where the reflections from each impedance mismatch is small. Keeping each section of an electrical length equivalent to $\lambda_g/4$ additionally creates destructive wave interference of the reflections from neighbouring sections, further reducing their effects at the output and input. The number of sections corresponds to the performance, as measured by Γ and the bandwidth over which it is minimized, but compromises in performance can be made to reduce the number of sections. A common compromise is to accept some level of ripples in Γ over the matched frequency band, and thus reducing the number of transformer sections. By using Chebyshev-polynomials, it is possible to optimally place the zeros of the transfer function in the Gamma-plane to keep the height of in-band ripples equal, and achieve a wider bandwidth under the acceptable level [17].

Another matching method is to use a linear or triangular taper to gradually change from one impedance to another, usually over a length of transmission line of at least one guided wavelength λ_g, or more. Linear tapers are generally inferior in performance to Chebyshev multisection transformers, having a higher Γ, but they are very simple to implement and optimize, and sometimes the performance is acceptable in that context. The linear taper is defined as a linearly changing impedance. In waveguide that corresponds to a linear change, but in microstrip it deviates slightly from that. It is however a common approximation to implement it as linear change in width of microstrip.

4
Design

Two waveguide terminations were studied, and will be presented in this chapter.

The first design, described in section 4.1 utilizes a waveguide-microstrip transition or an E-field probe, to pick up the incoming waves from the waveguide and lead into a resistive thin-film microstrip deposited on a single 65 μm thick crystalline quartz substrate. This design focused on the frequency range 270-370 GHz, and aimed to achieve a reflection ratio of below -26 dB.

The second one, described in section 4.2, consists of bilateral finlines tapering together into a substrateless slotline, then coming together in a short circuited end. It's a single structure made of 30 μm thick high-resistivity silicon, with one broadside and all sides of the structure coated in resistive thin-film TiN, leaving the substrate on the other broadside as uncovered silicon. This design focused on and achieved the whole useable waveguide band, 210-370 GHz.

Both terminations were designed for waveguide size of 760×380 μm, designed for the frequency range of 210 - 370 GHz of ALMA bands 6-7, although only the finline structure covers the whole waveguide band. The cut-off frequencies for modes TE_{10} and TE_{20} of this waveguide size are respectively 197.2 GHz and 394 GHz, as calculated by formula 3.21, showing the lower and upper limits of its single mode propagation in the fundamental mode.

Both terminations are designed to use a resistive thin-film as the lossy conductor in which the RF energy is dissipated, aiming for a sheet resistance of 30 $\Omega/\square$. A range of sheet resistance values can be fabricated, as discussed in 3.2, but this one is chosen based on in-house experience as one that is straight-forward to achieve and can be produced consistently to a good accuracy. To put the resistivity in perspective to known conductors, referring to formulas in 3.1, its bulk resistivity at DC is in the range of 2.5×10^5, compared with Au at 4.1×10^7, making it certainly an unfavorable conductor if low losses are desired, while still not being high resistivity.

An indispensable tool to design RF hardware is 3D electromagnetic full-wave simulators, integrated with a 3D CAD software, the one used for this project is Ansys High Frequency Structure Simulator (HFSS). The design process starts with finding reasonable building blocks and elements for the use case, such as transmission lines, material qualities, components and impedance matching methods, then calculating physical dimensions and electrical characteristics according to theory, and then sketching them in the 3D CAD software. The software can then simulate its performance and calculate the relevant performance metrics, such as in this case the reflection coefficient, S_{11}. The user can then define an optimization strategy, choose which parameters such as widths and lengths should be modified and over which range, to achieve a better performance.

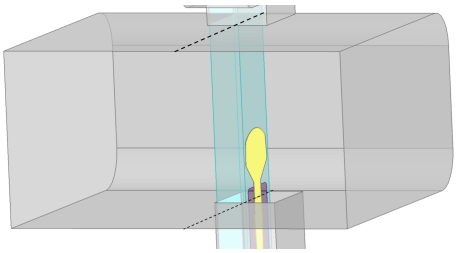

Figure 4.1: E-probe based design. Gold shown in yellow, crystalline quartz substrate in transparent blue, TiN resistive thin film in purple. Splitblock plane on waveguide shown in dashed lines

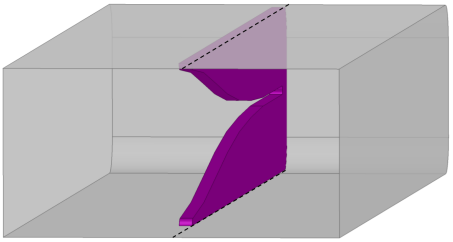

Figure 4.2: Finline based design. TiN resistive thin film shown in purple. Splitblock plane on waveguide shown in dashed lines

Figures 4.1 4.2 present both designs in their final form, as seen looking into the waveguide as it is described in section 3.3.6. Since this is a termination, the waveguide is shorted at the back. The end-corners of the backshorted waveguide are rounded, since they are milled with CNC machining. The smallest available tool diameters useful for such milling are on the order of 60 μm, which sets the limit on the radius of the end corner fillet. Above that size range however, the fillet radius can also be a tuning parameter for the electromagnetic behaviour of the backshort.

4.1 E-probe based design

The electric-field probe consists of a gold conductor on a dielectric substrate, described further in section 4.1.4. It couples to the EM fields in the waveguide and leads the RF energy into a resistive termination where it is dissipated, described in section 4.1.3. This structure sits inside a substrate channel, placed in the correct location in the larger waveguide structure, described in section 4.1.2. The whole design has several degrees of freedom, but certain constraints are well defined from the start, described in next section 4.1.1.

4.1.1 Initial design constraints

Using the splitblock manufacturing method, based on the ability to split a waveguide along the broad-wall's centerline as described in 3.3.6, the larger input waveguide leads into a smaller waveguide, here referred to as the substrate channel. The width of the substrate should not be so large that it becomes a waveguide by itself, i.e. supporting propagating substrate modes. For some safety margin, setting the frequency cut-off at 395 GHz, following formula 3.21, the widest allowed substrate is found to be 180 μm. The substrate will need to sit in a substrate channel with some gaps on the sides, so somewhat narrower than 180 μm is preferred.

To maximize power transfer from the TE_{10}-moded waveguide to the microstrip termination, an E-probe with a very high S_{21} or coupling-factor over the desired

bandwidth will be required, and an output impedance adjustable within the range of the resistive microstrip line widths that fit on the substrate.

The substrate material for this design is 65 μm thick crystalline quartz. Its relative electrical permittivity is $\varepsilon_r = 4.43$. It is mechanically strong, and has seen use in many other designs for cryogenic operation and terahertz applications, for its low loss-tangent and reliability through thermal cycling. At millimeter-frequencies, the sizes of many components become very small. The relatively low permittivity of quartz is appealing in this regard, as it keeps the design larger which will make it easier to process and handle. An E-probe designed by [34] uses quartz and achieves an impedance very close to pure real, and presents designs on other higher permittivity substrates such as Silicon and Gallium-Arsenide which have some reactive components and approximately 2/3rds of the size of the quartz-based one.
From formulas 3.5 and 3.17, a higher relative permittivity would enable a higher $\frac{R}{Z}$ ratio, resulting in a theoretically attenuation per unit length. This could potentially result in a physically smaller load, which might be desirable at lower frequencies, but with the already miniature size in question here, a physically larger and more mechanically robust structure makes the manufacturing and mounting more convenient.

A suitable conductor material is gold, Au, to be deposited by electron beam evaporation to a thickness of 500 nm. It is also a common choice for cryogenic applications and high frequencies. Additionally, experience shows that depositing a thin layer of titanium first improves adhesion between the gold and quartz, here a 10 nm such layer was used.

The material for the resistive thin-film is Titanium-Nitrogen, TiN. The nitrogen acts as a pollutant which reduces the conductivity of the titanium. They are mixed by sputtering titanium in a nitrogen gas rather than a near-vacuum, the nitrogen enters the titanium crystal as it's forming, and reduces its conductivity, as described in section 3.2. The goal sheet resistance was 30 $\Omega/\square$.

4.1.2 Substrate channel in waveguide

The quartz substrate carrying the E-probe and resistive microstrip sits in a substrate channel, which is a waveguide cavity from the input waveguide, perpendicular from its propagation axis and terminated in a short. The substrate itself sticks out of the substrate channel, suspended across the input waveguide. The location of the hole is so that the conductor-side of the substrate, where the E-probe sits, is in the center of the floor, at the peak of the voltage distribution of the TE_{10} mode.

Enclosing a microstrip changes its effective dielectric constant, and so its impedance. Generally it is desirable to have the walls and ceiling far enough away to have minimal coupling with the electric field, to minimize this effect to simplify design. Relative to the substrate thickness, a rule of thumb recommended for microstrip design is that the distance to ceiling should be eight times the thickness, and the distance to walls should be five times the thickness [19]. But in the detailed study on E-probes presented by Kooi et al. [34], they find that best bandwidth is achieved by having the the substrate channel height not more than twice the the thickness of the substrate. The starting value for optimization was with the height

exactly twice the thickness, and exploring values to both sides in the simulation it was found to best at 70 μm, compared to the 65 μm substrate thickness.

The distance to the backshort, the bottom end of the terminated waveguide, is another important factor. Here it is measured from the center-line of the substrate, as indicated in figure 4.4. Given a centered placement of the substrate in the substrate channel, it determines where the E-probe sits in the standing wave. Following the theory and dimensions presented in [34], the starting value for optimizations was 190 μm, but values ranging from 140 to 350 were explored, and best simulated performance was at 188 μm. One way to think of the function of the E-probe with regards to its placement against the backshort is that it should be located on the peak of the first standing wave, where the voltage peak is the highest. For the center frequency here, 320 GHz, which in the 760x380 μm waveguide gives a TE_{10}-mode $\lambda_g/4 = 297.5$ μm, which should be the backshort distance according to that understanding. If this distance is shorter than $\lambda_g/4$, it rotates the electrical short around the smith chart and turns it into an inductive shunt tuning element, as explored in Kooi et al. [34].

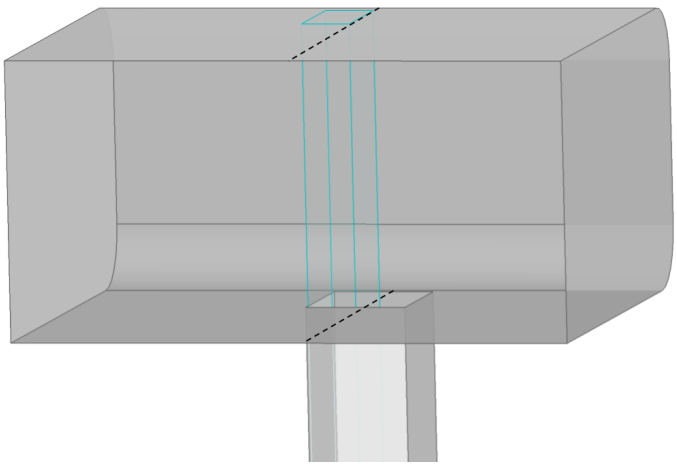

Figure 4.3: Looking into the input waveguide, showing the placement of the substrate channel in the floor, outlines of the substrate in blue, and the plane of the splitblock in dashed lines

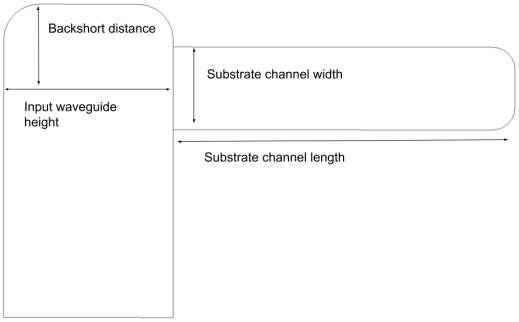

Figure 4.4: Top-down view on split plane of waveguide structure, showing location and sizes of the substrate slot

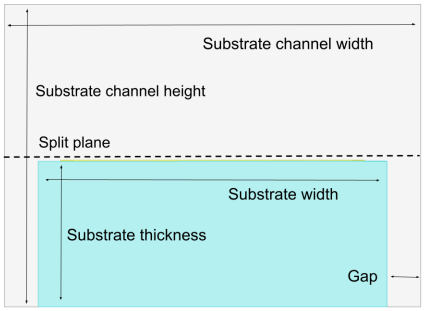

Figure 4.5: Dimensions and placement of quartz substrate in channel. Split plane indicated with dashed lines

Dimensions	**Initial Values [μm]**	**Optimized Values [μm]**
Backshort Distance	190	188
Input Waveguide Height	380	-
Substrate Channel Width	190	185
Substrate Channel Length	1000	765
Substrate Channel Height	110	135
Substrate Width	180	155
Substrate Thickness	65	-
Gap	10	15

Table 4.1: Waveguide and substrate channel dimensions

The table lists the sizes and dimensions shown in the previous figures. The dimensions of the input waveguide height, and the substrate thickness, were decided by other factors and not subject to optimization.

4.1.3 Design of the resistive microstrip load

The load is a length of resistive thin-film conductor, where the RF energy gets dissipated by ohmic losses. While at lower frequencies such a load can be essentially a resistor connected to ground, at the frequencies used here this would be impractical. The quartz substrate does not yield itself well to drilling via-holes for grounding, due to being brittle and hard to drill such small holes in at this scale. Bonding wires to circuit ground add a bandwidth limiting inductance, and it complicates the design, fabrication and mounting unnecessarily if it is at all avoidable, by adding more steps that involve manipulating microscopic elements with high precision. So

a floating load is better suited, i.e. one that is not physically connected to the circuit ground since can be manufactured to a high degree of accuracy and precision using lithographic methods, and integrates well with the E-probe itself and the suitable substrate.

By depositing a thin layer of Titanium mixed with Nitrogen, it is possible to control the conductivity and thickness of the metal within a certain range, and in turn its sheet resistance, as explain in section 3.2. With the fabrication method and equipment used, it has been found that a sheet resistance of 30 $\Omega/\square$ can be reliably manufactured with high repeatability, so it is chosen as the sheet resistance value of the load. This sheet resistance value results in an approximately 140 nm thick film.

4.1.3.1 The width of the load

From the theory explained in 3.7 ($\gamma = \alpha + j\beta$, with $\alpha = 2R/Z_0$) it is seen that a narrower load would have higher resistance and thus higher attenuation. Another thing to consider however is the bandwidth of the matching and power transfer, as described in section 3.9. As the load becomes wider its impedance becomes closer to being pure real. A narrow, resistive microstrip has a significant series capacitive reactance which will limit the bandwidth of the matching and thus the power transfer between probe and load. Optimizing the performance of this design becomes about finding the balance between attenuation per length unit on one hand and impedance matching over a broad band against the reactive part of the load, on the other. With the small physical dimensions inherent with those frequencies, the slight increase in length that results from the greater width is not of great consequence for this use case and might even benefit fabrication and mounting in the waveguide.

To map how the width of the load affects its characteristic impedance, with the previously described substrate and resistive thin film, it is plotted here based on the calculations of microstrip characteristic impedance and transmission line characteristics described in 3.17 and 3.4, for the range of widths that are considered. The plots show first the real and imaginary parts of the characteristic impedance, and then the argument of the complex number, normalized over π, for 30 $\Omega/\square$ sheet resistance microstrip, at the center frequency 320 GHz, on 65 μm thick $\varepsilon_r = 4.43$ quartz substrate. The real part of the characteristic impedance closely follows a lossless microstrip, but the resistivity adds a series capacitance seen as a negative imaginary component.

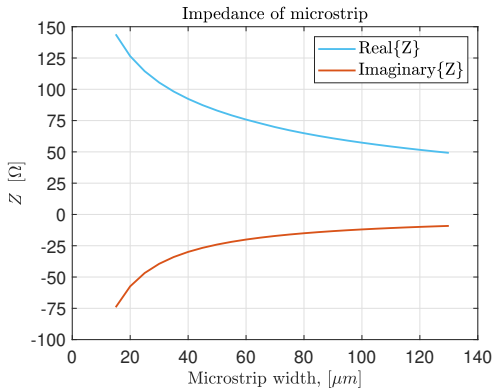

Figure 4.6: Real and imaginary microstrip characteristic impedance v.s. width, of the lossy microstrip at 320 GHz

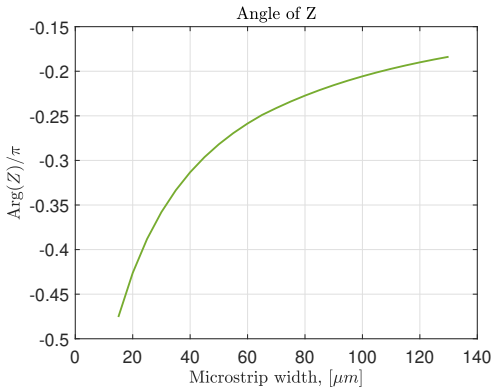

Figure 4.7: The angle of the characteristic impedance normalized over π v.s. width of the lossy microstrip at 320 GHz

This makes it clear, following equation 3.9 and the surrounding theory, that a wider load with the cost of added length is a worthwhile tradeoff. Setting the width at 120 μm gives a characteristic impedance $Z_c = 51.6 - j9.9\Omega$, for a lossy microstrip if it were not enclosed in a substrate channel. As mentioned in section 3.3.4, a narrow enclosure will affect the impedance in ways that no closed-form formulas exist to calculate, and the established method is to use numerical computation such as with 3D fullwave simulators to approximate its value. But the change of the real and imaginary components of the impedance with the width of the resistive microstrip can be reasonably assumed to be similar, whether enclosed or not.

4.1.3.2 The length of the load

The impedance Z_{in} seen looking into a terminated transmission line can be calculated with the telegrapher's equation, 3.8. It can be seen from there that as the product of loss and length of the transmission line increases, the impedance looking into it converges to its characteristic impedance following $tanh(\gamma l)$, if $Real\{\gamma\} \neq 0$. So even if the the microstrip line is terminated in an open circuit, or that is, a load impedance $Z_{Load} \to \infty$, at the right length l for a given loss, this becomes irrelevant and $Z_{in} \to Z_0$ anyway. Plotting $tanh(\gamma l)$ for a 120 μm wide microstrip line at 320 GHz, and a range of lengths demonstrates this clearly:

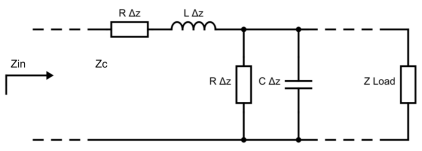

Figure 4.8: Circuit model of the beginning, end and one Δz segment of a lossy transmission line, showing the input impedance, the characteristic impedance and the termination load

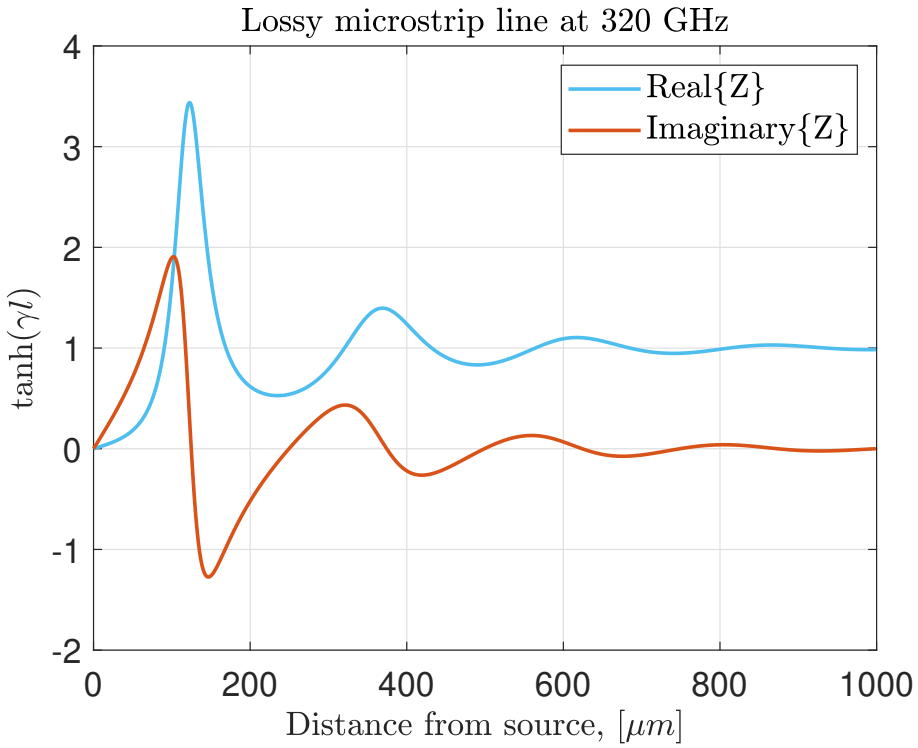

Figure 4.9: Plotting $tanh(\gamma l)$ of the telegrapher's equation, for a γ of the 30 $\Omega/\square$, 120 μm wide resistive microstrip line at 320 GHz, over a range of lengths

Where $tanh(\gamma l)$ is from the telegrapher's equation:

$$Z_{in} = Z_0 \frac{Z_L + Z_0 \tanh(\gamma l)}{Z_0 + Z_L \tanh(\gamma l)}$$

Where Z_0 and γ are the transmission line's characteristic impedance and propagation constant respectively, and l is its length or more generally position along its length. This shows that for a lossy transmission line, i.e. $Real\{\gamma\} = \alpha \neq 0$, yields the convergence $\tanh \gamma l \to 1$ with increased l, leading to $\frac{Z_0 + Z_L \tanh \gamma l}{Z_L + Z_0 \tanh \gamma l} \to 1$ which ultimately leads to $Z_{in} \to Z_0$, or the input impedance converging to the characteristic impedance regardless of the termination. From this, the initial length of the load is chosen to be 800 μm, but the optimization will explore values down to 630 μm. Higher sheet resistance or narrower microstrip would achieve a $tanh(\gamma l) \approx 1 + j0$ at lower lengths due to having higher $Real\{\gamma\}$, but would suffer from the problems described in the previous section.

4.1.4 Probe design

One of the probe designs presented by Kooi et. al [34] shows nearly pure-real impedance, on quartz substrate and for a similar range of frequencies as in this application. This is very promising, as explained in section 3.3.1 on power transfer. The load impedance is however not pure real, so some modifications are required for a good match. A variation of that probe, presented by [15] has more degrees of freedom in extra width for optimizing the performance against the impedance of the resistive and slightly series-capacitive microstrip load.

It was found through simulation experimentation that low probe impedances, in the range of 25 to 30 Ω resulted in great variations in the argument of the impedance over the frequency, while for higher impedances around 50 to 60 Ω or higher, similar magnitude variations of the imaginary part of the impedance had much smaller effects, as to be expected. As expressed in equation 3.7, a lower impedance would give higher attenuation, but that needs to be balanced out against the bandwidth of the impedance matching, for which variations in the imaginary part of the impedance are detrimental.

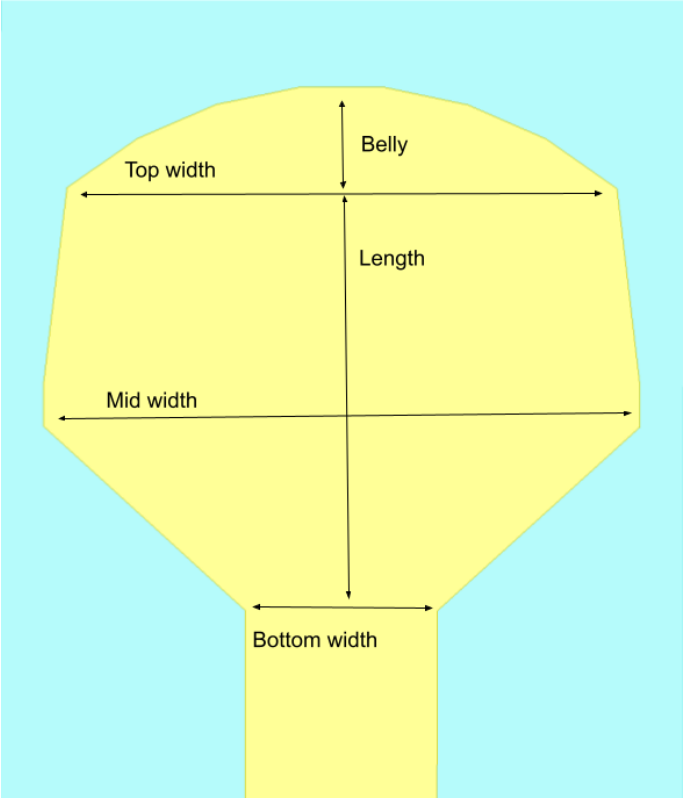

Figure 4.10: Chosen shape of E-probe on suspended substrate, after optimization

The following table shows the dimensions of the probe on the picture, after optimization with the resistive microstrip line including the matching taper described in the next section, 4.1.5. Since the probe is made on the substrate using lithography, it can be manufactured to a high spatial precision and accuracy.

Parameter	Value	Unit
Belly	22	μm
Top Width	124.6	μm
Mid Width	137	μm
Bottom Width	43.5	μm
Length	101	μm

Table 4.2: Dimensions of E-probe, after optimization with resistive microstrip termination

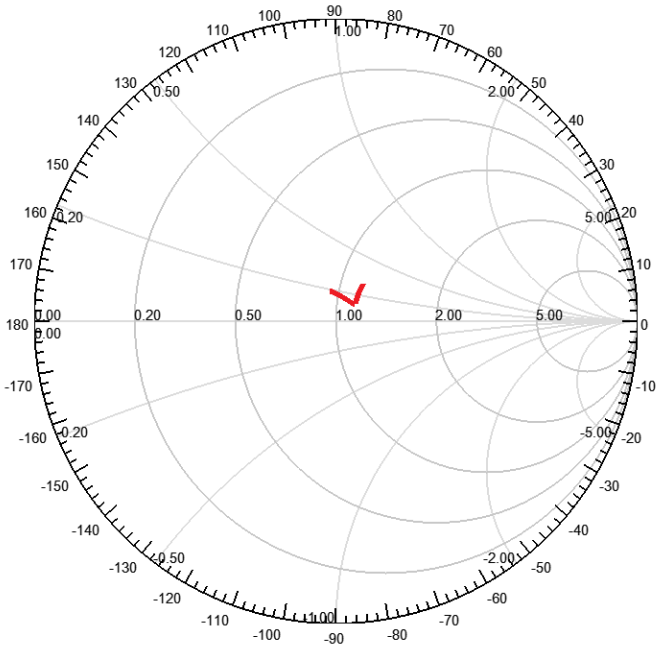

Figure 4.11: Output impedance of E-probe on smith chart, normalized to 50 Ω

The figure above shows how the impedance of this probe structure appears on the smith chart, it is seen that its impedance is close to being a conjugate of the calculated first approximation of the characteristic impedance of the load, at $Z_{C,Load} = 51.6 - j9.9\Omega$, as described previously in section 4.1.3.1. Minor variations through the frequency range remain however.

Output Impedance [Ω]	270 GHz	320 GHz	370 GHz
Real{Z}:	47.4	56.17	58
Imaginary{Z}:	9.5	6.47	14.81

Table 4.3: Impedance of E-probe

The length and width of the E-probe are important features, but a very important factor in its output impedance turned out to be the width at the base, or the bottom width.

Other methods of tuning the impedance E-probe as it appears from the input of the waveguide, include shifting it against the backshort, adding a floating conductive counter-element elsewhere on the substrate, a deeper air-filled channel under the substrate to reduce the effective dielectric constant of the substrate and thus modify the impedance. These methods were explored preliminarily but eventually turned out to not be necessary.

4.1.5 Probe-to-Load matching

Direct connection between the probe and taper did not exhibit very good performance in simulations. The next step was to define a linear taper of Au between them, and also define a 5 μm overlap of the TiN and Au along its contact circumference, to both establish adequately low electrical contact resistance, and to ensure that it would be maintained through any minor misalignments in the lithography process.

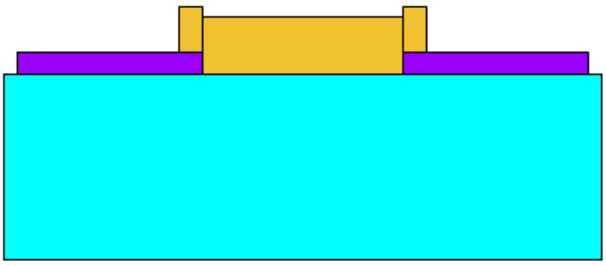

Figure 4.12: Cross-section of substrate showing overlap between the deposited gold shown in orange, and TiN shown in purple, to ensure low contact resistance and robustness to any lithography mask misalignments

Since the resistive microstrip load and the E-probe by itself present slightly different input and output impedances respectively, which also change through the optimization process, a convenient way to match them together is to use a simple triangular matching taper. The impedances of both the load and the termination are difficult to evaluate precisely, whether analytically or numerically, and thus need to be optimized together as one structure after the initial and approximate sizes are decided.

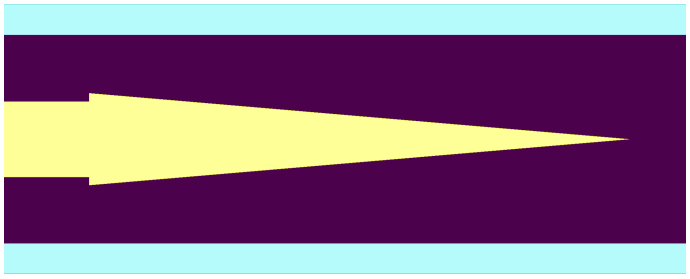

Figure 4.13: Top-down view in split plane, showing linear taper of length 303 μm, matching between probe and resistive microstrip termination

The linear taper is generally not the most effective impedance matching taper, having a greater length than the other approaches, and higher reflection coefficient than the Chebyshev multi-section transformer. It is however very simple, its geometric structure being defined only by base-width and length, so for very small mismatches between impedance values that are hard to pin down exactly, like in this case, and for optimization purposes, it can serve very well. Lengths of the taper were explored in optimizations from 150 μm to 600 μm, but the best performance found there. The base-width was likewise explored from being more narrow than the probe lead which is 43.5 μm, to being wider up to 100 μm, but 53.5 μm showed the best performance.

Taper Width [μm]	**Taper Length** [μm]	**Taper electrical length at** f_c [βl]
53.5	303	$\sim \pi$

Table 4.4: Dimensions of optimized linear taper

The table lists the width of the base of the taper, and its length. It also lists its electrical lengt at the center frequency, 320 GHz.

The best performance was found experimentally with a taper length of 303 μm, and width 53.5μm, against the probe base width of 43 μm. This is somewhat surprising. As described in Pozar [17], the lowest reflection coefficient $|\Gamma|$ from such a taper is achieved at electrical length $\beta l = n2\pi$ for $n = 1, 2...$, but 303 μm here corresponds to approximately $\beta l \approx \pi$, or half a wavelength at center frequency. It is therefore uncertain whether this taper is performing as an impedance match, or increased contact surface between Au and TiN, or a wave-launcher into the resistive film.

4.1.6 Simulated performance of optimized E-probe based waveguide termination

After optimization of the probe dimensions and its placement within the input waveguide, the performance shown below was achieved. The performance metric for a waveguide termination is its S_{11}, or reflection coefficient, how much of the input power gets reflected back. The design goal was to achieve -26 dB over the frequency band of 270-370 GHz. At the band edges, the S_{11} is

270 GHz	**370 GHz**	**FBW < -26 dB**
-27 dB	-28.8 dB	0.33

Table 4.5: S_{11} and bandwidth of E-probe based waveguide termination

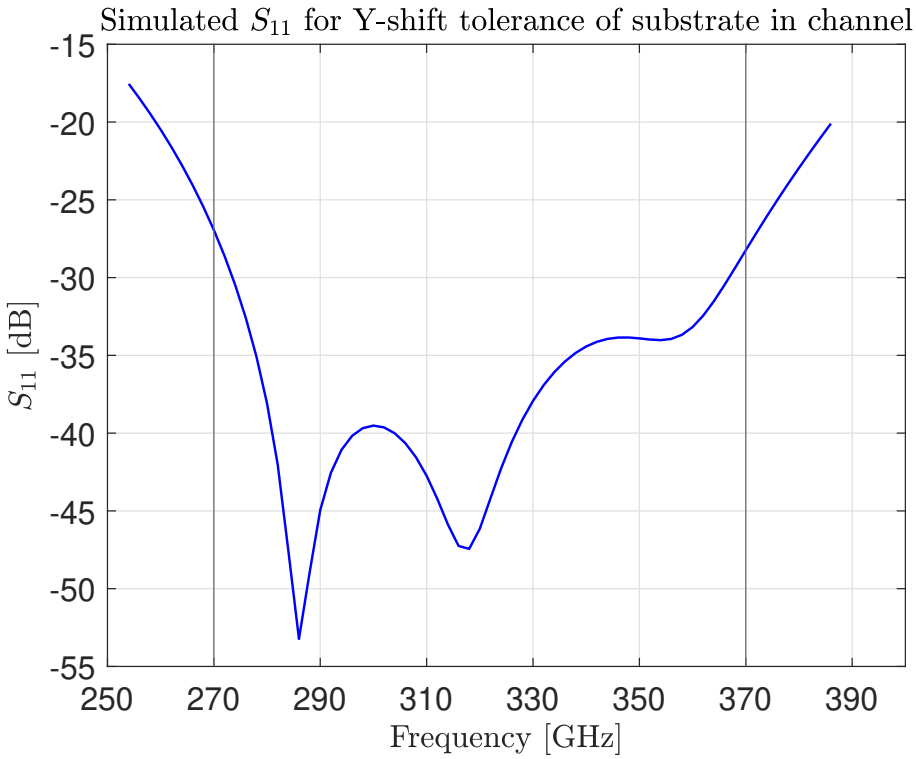

Figure 4.14: S_{11} response of the E-probe based waveguide termination, after optimization. 270-370 GHz range delimited on the graph, showing performance of under -26 dB across the band. S-parameter normalized to the input impedance of the waveguide.

4.1.7 Initial investigation of tolerances

Simulated performance of this waveguide termination exceeded the performance specifications. Preliminary assessments of mounting and fabrication tolerances however showed that it was sensitive to a placement of the substrate within the substrate

channel up to a very high degree of precision, which would pose challenges in mounting the cip. In particular, shifts along the length of the substrate channel, in the Y-direction.

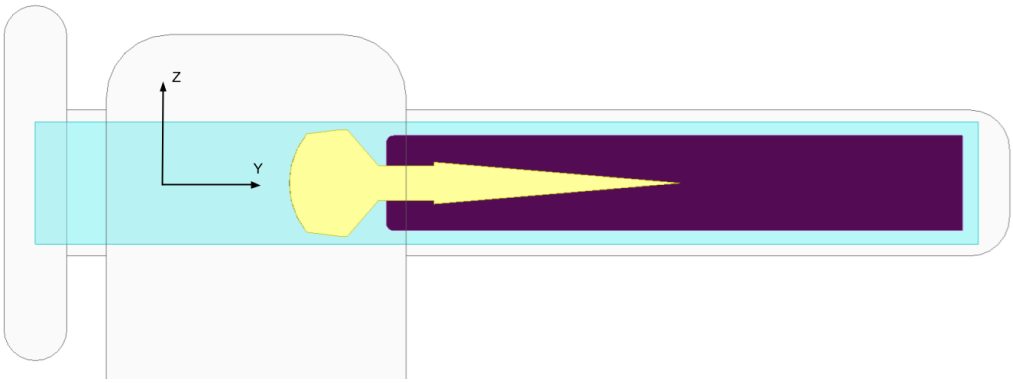

Figure 4.15: E-probe based waveguide termination, mounting assistance cavity on the left side. Seen in top-down view on split-plane

Attempts to mitigate this focused on reducing discontinuities in the microstrip line directly on top of the edge between the input waveguide and the substrate channel, by letting some of the resistive material stick out into the input waveguide, and stretching the lead from the probe further into the substrate channel. This reduced the sensitivity somewhat, but performance is still highly dependent on the mounting accuracy.

4.1.8 Tolerance analysis

Precision fabrication is generally needed to fabricate components at such high frequencies. The fabrication steps involved, described in more detail in chapter 5, are: depositing the metal on the conductor using lithographic methods, dicing the substrate with a saw into rectangles of the right length and width, milling the waveguide out of a solid block of aluminum, and then mounting the substrate chip in the right place in the substrate channel. Each of those steps introduces dimensional errors to the structure to different degrees, no matter how carefully performed. An accurate assessment of the potential inaccuracies is hard to state with absolute confidence, but rough estimates to guide tolerance analysis can be made based on experience, shown in the following table.

With the relatively high accuracy of the lithography compared to other sources of inaccuracy, analysing the tolerance of the performance to the other sources will be prioritized. Since the installation is done by hand under a microscope, it has a lot of potential as a source of error in the YZ plane as shown in figure 4.15. With the mounting method, initially using wax to fix it in place, it can however be re-aligned.

Fabrication step	**Potential error** $[\pm\mu m]$
Lithography (Au and TiN)	<0.1
Substrate dicing	5
Waveguide CNC milling	5
Chip mounting	5

Table 4.6: Estimates of potential dimensional errors in fabrication

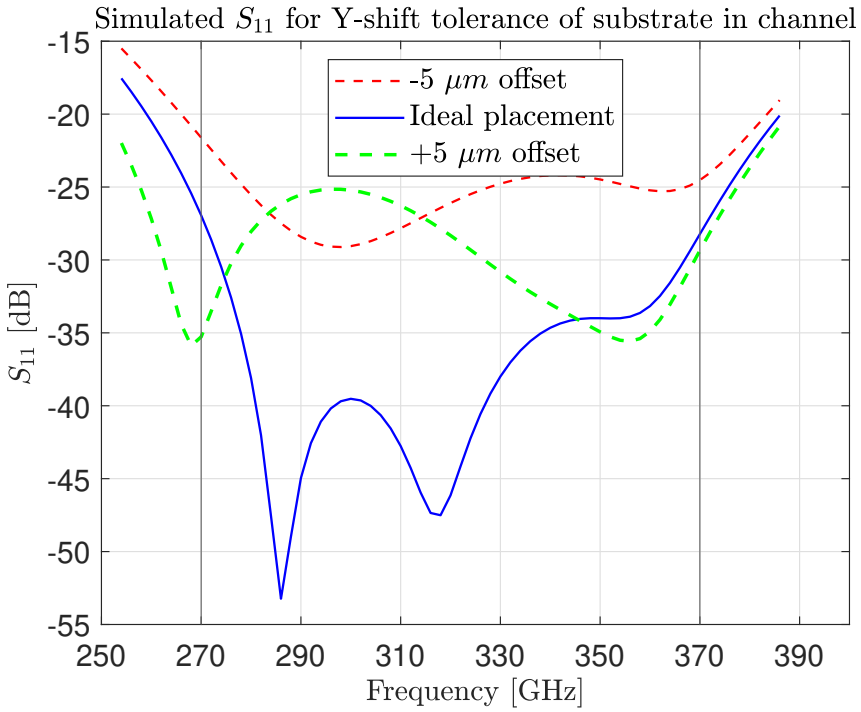

Figure 4.16: +/- 5 μm shifts in the Y-direction

Figure 4.16 above shows how the S_{11} is affected by shifting the substrate chip $\pm 5\mu m$ along the Y-direction. Some performance is retained, but decreases significantly to barely -24 dB, and for the -5 μm shift, the bandwidth is reduced.

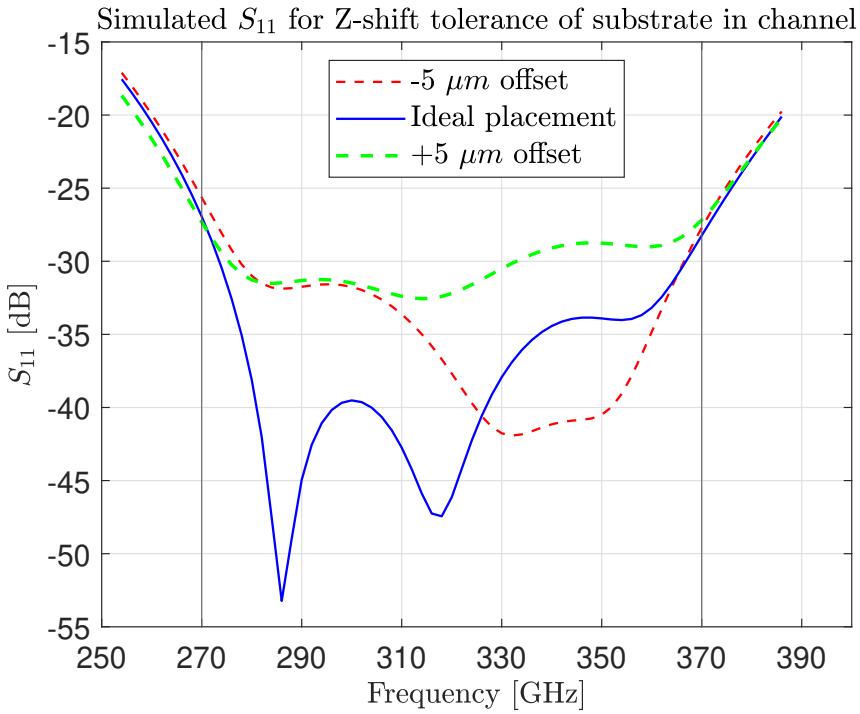

Figure 4.17: +/- 5 μm shifts in the Z-direction

Shifting the substrate chip in the Z-direction within the substrate channel makes the gaps asymmetric. As understood from previous sections about microstrip impedance 3.3.4, if conductive sidewalls are close enough to significantly interfere with the electric field, then they affect the impedance. As the simulation show, this affects the performance, but not as much as the Y-shift. Performance remains below -26 dB across the band.

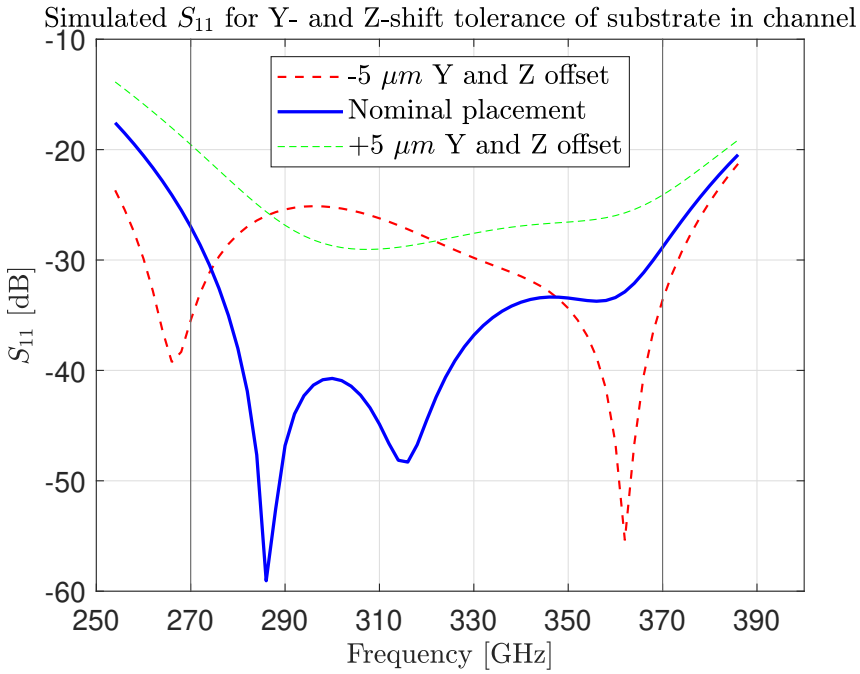

Figure 4.18: +/- 5 μm shifts in the Z- and Y directions

The worst result would then be to combine both shifts, +5 μm in both Y and Z on one hand, and -5 μm in both Y and Z on the other, as shown on figure 4.18 These results show that adding some features to the design to facilitate accurate mounting in the waveguide would be highly benficial, and also demonstrates some of the difficulties of manufacturing instrumentation for such high frequency ranges.

The added features to the design were small 10×10 μm wide squares as alignment marks. They should be equally far away from the edges between the input waveguid and the substrate channel. This will be mounted in a microscope, and the substrate is transparent, so it is important that the squares be large enough to be seen clearly through the microscope. Another feature to help with mounting is the alignment cavity on the left hand side of the figure below, to more easily fit narrow-tipped tools to shift the substrate around. The floor of the cavity is also 10 μm lower than the floor of the substrate channel, to add another sharp edge that can be used for alignment.

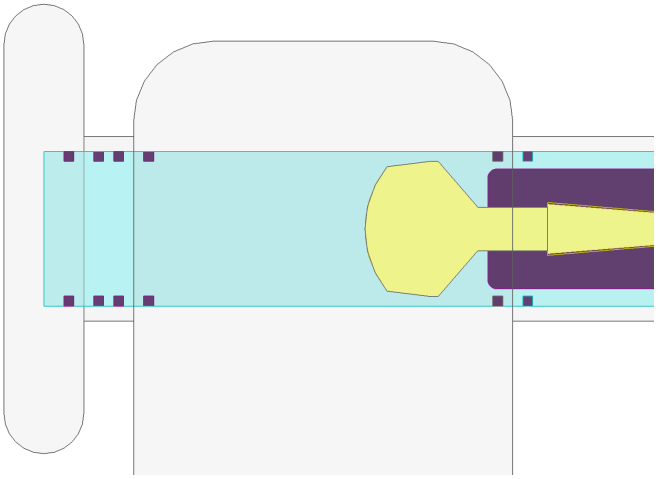

Figure 4.19: E-probe termination in its final form, showing TiN alignment marks on substrate, mounting assistance cavity to the left

4.2 Finline based design

The finline-based waveguide termination consists of a slab of 30 μm thick high-resistivity silicon dielectric, of relative permittivity $\varepsilon = 11.7$, inserted parallel to the electric field in the waveguide and along the propagation direction. The finline transmission line is known to be inherently broadband, but lossy, demonstrating both conductor and potentially radiative losses. It can form a physically large structure relative to wavelengths, which makes it convenient for fabrication and mounting into a sub-millimeter sized waveguide. At the beginning of this project it was uncertain what bandwidth and performance might be achieved in a reliably way, but the goal was to cover the whole frequency range of the waveguide's fundamental mode, which corresponds to ALMA bands 6-7, 210-370 GHz, and achieve as low Γ as possible.

As described in section 3.3.7, the characteristic impedance of a finline depends on the separation gap and the thickness of the substrate. The lowest impedance and highest loss is achieved with the smallest separation distance. To achieve impedance matching the separation distance must be decreased slowly from the waveguide's full height of 380 μm using a smooth impedance matching taper, and then lead it in a straight 20 μm gap far enough to achieve a similar $Z_{in} \rightarrow Z_0$ transmission line effect as was discussed in 4.1.3, so it can be terminated in a short circuit. The short circuit also acts as mechanical support, so the structure can be manufactured and mounted in the waveguide as one solid piece

The dissipation of the energy is achieved by using a resistive thin-film conductor, of sheet resistance $R_{\square} = 30\ \Omega/\square$, which is sputtered on to the top layer and edges of the finline, leaving one side as exposed silicon. Additionally the finline structure is separated from the waveguide ceiling and floor by a small gap, 5 μm, to make facilitate mounting and to not rely on physical contact for electrical grounding.

4.2.1 Initial design constraints

The substrate is shaped using plasma etching. This puts a constraint on how narrow the narrowest gap in the slotline can be, as the plasma etching effect is nearly line-of-sight, so the walls that make up the slotline gap on finline chips off-center on the wafer might get unevenly etched. For this fabrication the lower width limit was set at 20 μm. Although during the processing it was found it could potentially be narrower, but the impedance and attenuation achieved at 20 μm was sufficient.

A 30 μm thick silicon substrate was selected for this, as it is relatively easy to shape in this way to a good precision, but should prove to be mechanically strong enough for mounting, according to in-house fabrication experience.

Since this design is intended for operation at cryogenic temperatures it is not feasible to rely on the lossy properties of silicon as a dielectric like was done in a waveguide termination by Beuerle et al. [13], since the dielectric loss tangent of silicon is not reliably high at cryogenic temperatures, as characterized in [38]. Instead, this termination will utilize resistive thin-film, which is known to have a

nearly constant level of ohmic losses, through the temperature range from room temperature to cryogenic.

The sheet resistance 30 $\Omega/\square$ is chosen for the same reasons as in the E-probe based design, something which is possible to consistently reproduce to a good precision with standard clean room methods.

4.2.2 Impedance and matching

The most critical aspect with regards to minimizing the reflection coefficient is the impedance match between the input and the termination. The finline structure with its lossy conductor must closely match the impedance of the waveguide itself. The attenuation is greater at low impedance, since more current flows through the lossy conductor, but the transformation between the impedances needs to be highly effective. This suggests to use a long, smooth tapering of the gap width, from a width close to the full waveguide height and down to the narrowest gap that is practical to produce. The resistive conductor in the taper is likely to achieve some attenuation, but the narrow straight finline at the end achieves the most per length unit, since it has the lowest impedance.

The impedance of a full-height waveguide is taken to be approximately 400 Ω, but it is higher at the lower frequency limit. The impedance of a finline varies with the separation between the fins, becoming lower with a narrower gap, and empirically derived formulas exist to approximate it, as referred to in section 3.3.7. It is however unusual to implement it with a deliberately resistive conductor, and the design formulas which assume negligible losses are thus not directly applicable in this context.

To acquire starting values on which to base the the taper, a straight finline structure as pictured in figure 3.3.7 with the resistive thin film was simulated in HFSS for the dimensions and specifications of the design constraints, and over a range of widths from the most wide of 370 μm to the most narrow, 20 μm. From the results of those simulated impedance values at the center frequency were chosen for each width, and a polynomial function curve-fitted to the data. From the inverse function, it is straight forward to calculate the physical dimensions of a taper from desired impedance values.

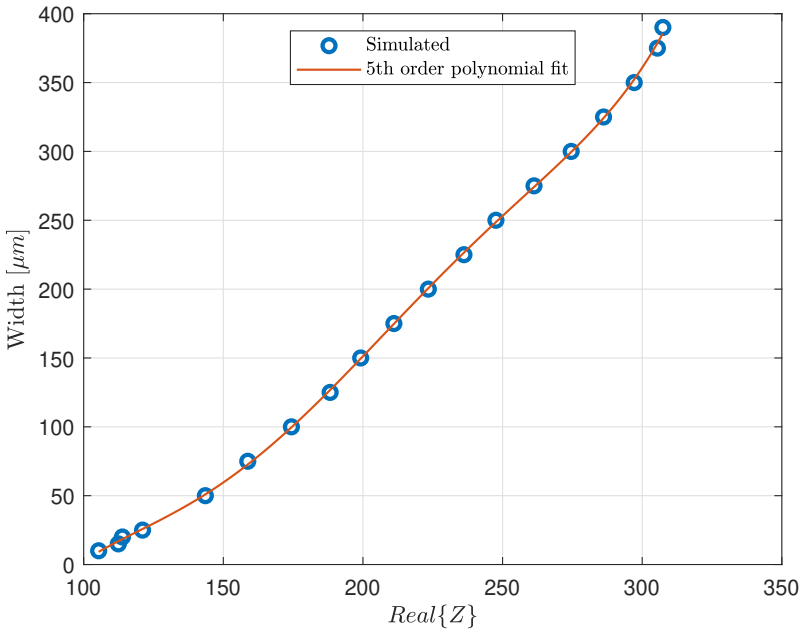

Figure 4.20: Plot showing the relation between finline gap widths and impedances, and interpolated with a 5th order polynomial

It is noteworthy on Fig. 4.20 that at the largest gap width simulated, 370 μm, the characteristic impedance was just over 300 Ω, still not close to the approximately 400 Ω impedance of the full height waveguide. At this gap width, and given the 5 μm space to the sides of the waveguide, the tips of finline structure are merely 5 μm thick, but made of a resistive conductor located in the peak of waveguide's electric field distribution. Additionally, with the conductivity of the TiN thin-film, its skindepth at the frequency range here as discussed in 3.2 is $\delta_s \approx 10t$ or almost ten times its thickness, so it is nearly transparent. The permittivity of the substrate is however very high compared to air, so the air-substrate interface has the potential to cause reflections.

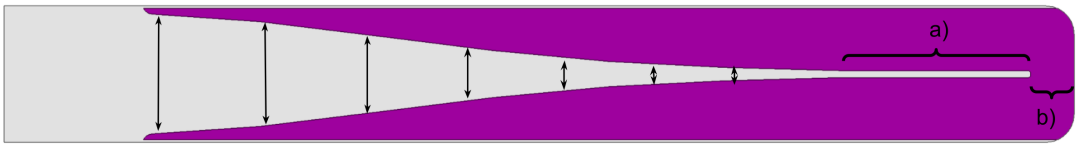

Figure 4.21: The finline structure shown in purple, in top-down view on the split plane. The gap widths indicated with arrows, at 285 μm long intervals. Section (a) is the substrateless slotline, and section (b) is the short termination

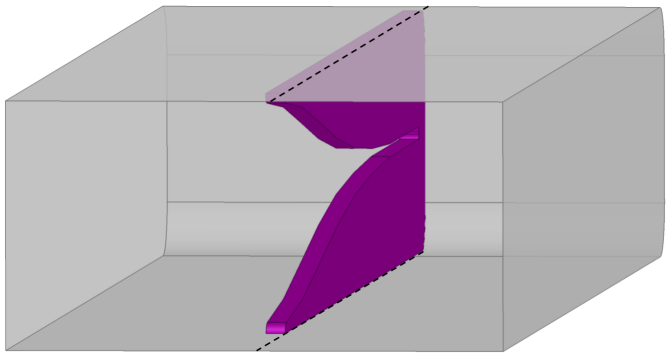

Figure 4.22: The finline-based waveguide termination as seen looking into the waveguide input, showing the finline in purple and the waveguide split plane in dashed lines

A Chebyshev matching taper of 7 sections was synthesized to match between the impedances at the largest gap and the narrowest gap, and translated into widths. To reduce discontinuities in an attempt to reduce reflections, the matching taper sections were smoothed out by using cubic spline. The sections of a Chebyshev taper are designed to be $\lambda_g/4$ long at the center frequency, where λ_g is the guided wavelength in the finline. An initial value for the guided wavelength λ_g was found by measuring the distance between peaks of current density in the simulated structure at the center frequency 290 GHz, and the mean finline gap width of 200 μm, and it was found to be $\lambda_g/4 = 250$ μm. Early attempts to increase low-frequency performance however showed that section lengths of $\lambda_g/4 = 285$ μm had a marked improvement.

Taper	**Gap widths of each section** [μm]						
Chebyshev	354.5	300	217	103.5	33	22.3	20
Optimized	336.0	300	234.0	149.40	73.60	33.80	20

Table 4.7: Comparison of finline tapers, Chebyshev matching v.s. after optimization. Gap widths measured from the tip, each section is 285 μm long

Table 4.7 lists the widths of the initial Chebyshev matching taper, at $\lambda_g/4 = 285$ μm section lengths, measured as shown on figure 4.21. The initial taper showed promising results, but further optimizations on the taper widths revealed that performance could be improved further, especially at the lower end of the band. The optimized taper starts somewhat more narrow, but narrows more slowly. The Chebyshev taper starts wider, and narrows rather fast around the mid-sections.

4.2.3 Straight narrow finline, or substrateless slotline

After the matching taper, the next part of the structure is the 20 μm wide gap finline, or substrateless slotline, marked as a) on figure 4.21. For this design, the optimal length was found to be 541 μm. The width was chosen based on experience of fabricating such a gap using available plasma etching methods. Narrower gaps might be difficult to etch with plasma, with the substrate thickness being 30 μm. A narrower gap would have lower impedance and higher attenuation, so it potentially could be shorter for the same effect. This transmission line has a similar effect as detailed in section 4.1.3 about the length of the resistive microstrip termination, in this case enabling a short-circuit termination, but making its input impedance look like its characteristic impedance despite that.

4.2.4 Short circuit termination

The finline structure is then terminated in a short-circuit, marked with b) on figure 4.21. In this design, the optimal length of this part was found to be 124 μm. Following the discussion of resistance 3.1, the length of this part determines the width of the terminating resistor, and thereby its resistance value. This makes the total length of the finline-based waveguide termination as shown on Fig. 4.21, 2660 μm long.

4.2.5 Simulated performance of finline-based waveguide termination

The performance of the finline-based waveguide termination was shown to be excellent across the whole waveguide band, with S_{11} < -37.5 dB above 215 GHz, and -26 dB at the intended lower frequency end of 210 GHz. Other aspects of it that are favorable are simple fabrication methods, and a relatively large structure which facilitates mounting in the waveguide.

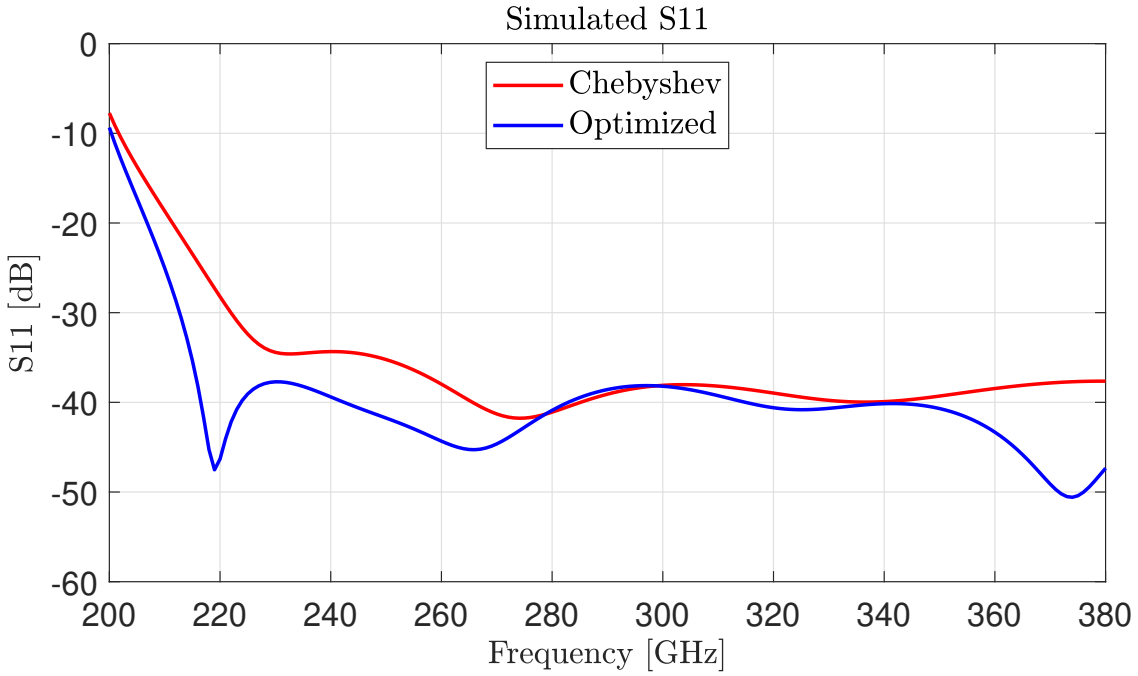

Figure 4.23: Comparison of S_{11} between the Chebyshev taper and after optimizing for lower frequency

The performance shown in the figure is very good, and covers the entire ALMA Bands 6-7, with S_{11} = -26 dB at 210 GHz, and then stays below -37.5 dB from 218 GHz and throughout. It is noteworthy that the initial attempt at the Chebyshev matching taper immediately showed very good performance, but a slightly less steep tapering extended the performance for a lower frequency.

210 GHz	218 GHz	380 GHz	FBW < -37.5 dB
-26 dB	-37.5 dB	< -40 dB	0.54

Table 4.8: S_{11} and FBW of Finline based waveguide termination

5
Fabrication

This chapter describes the fabrication process of both designs, and the waveguide blocks they will be mounted in for measurement and characterization.

Section 5.1 discusses the waveguide fabrication in more detail. With the small size of components and waveguides, it was convenient to make the waveguides for both components out of a single block. Since this design was made for 760×380 μm, which isn't one of the standard waveguide sizes, the measurements will require adaptation to the standard waveguide sizes on the VNA frequency extenders. Additional waveguides with built-in waveguide size transitions were milled into the block so that each design could also be measured natively at each of the neighbouring standard waveguides sizes, WR2.2 and WR3.4.

Section 5.2 deals with the fabrication of the E-probe and resistive termination is described in more detail. It was fabricated using standard clean room methods, on a quartz substrate, using TiN for the resistive microstrip termination and Au as the conductor for the E-probe itself. It was then diced by a dicing saw, using a 20 μm thick diamond blade, to shape the substrate into the right widths and lengths of individual chips.

Section 5.3 describes the fabrication of the finline based waveguide termination. It was fabricated by etching the shape out of a 30 μm thick high-resistivity silicon substrate. The silicon is provided from the manufactorer on a 300 μm thick backing structure also made of silicon, and they are separated by a 2 μm thick layer of SiOx insulator. After etching the shape, the backing structure is released into individual pieces and then covered with resistive thin-film TiN.

Both design take advantage of lithographic methods to place conductors on their substrates. It is an advantage that the fabrication uses well established and standard clean room methods.

5.1 Waveguide blocks

The waveguide blocks are fabricated in a split-block fashion. Following the theory outlined in section 3.3.6, it is possible to split a waveguide along the centerline of its E-plane, since no RF currents flow across the centerline and perfect electrical contact between the blocks is thus not critical for the travelling wave. Taking advantage of this makes the fabrication and mounting easier.

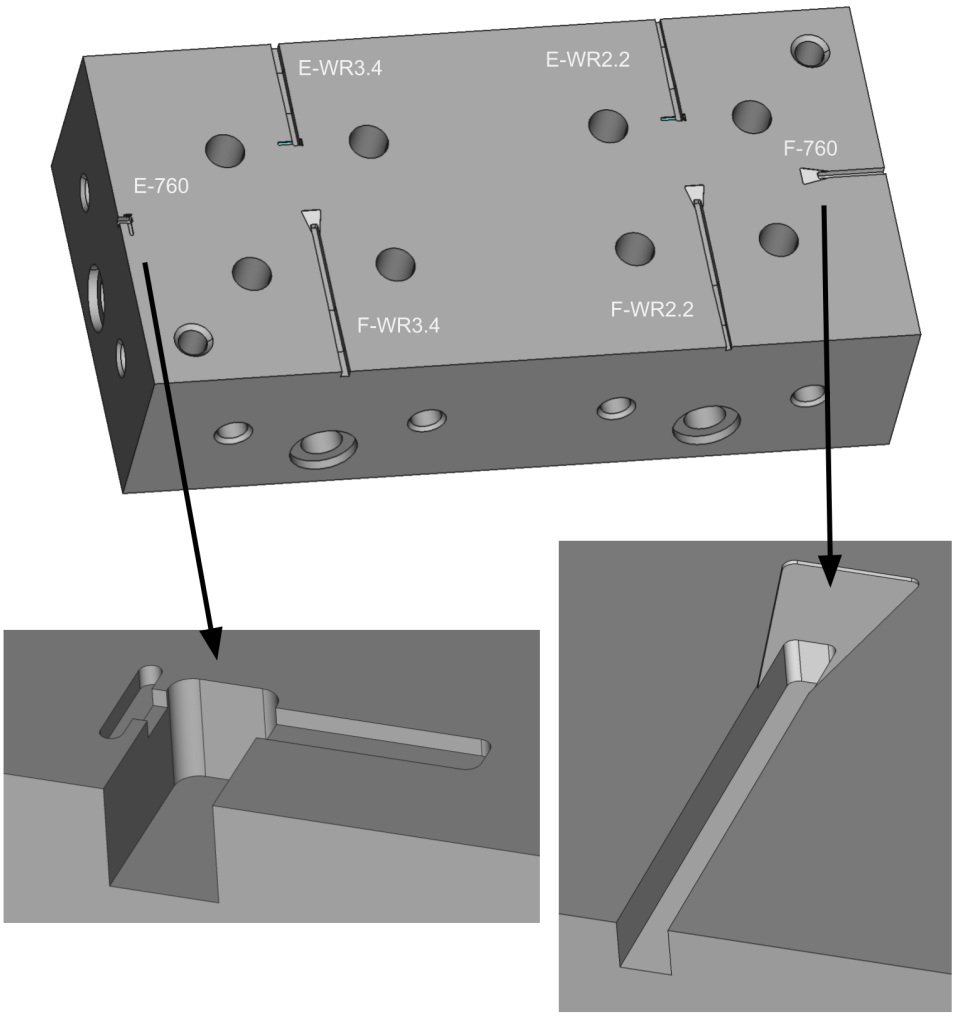

Figure 5.1: Lower half of splitblock, showing the 3 different variations of each waveguide, for each of the 2 termination designs. Also shown are holes for alignment pins which align the upper and lower block, and holes for screws which tigthen them together.

To make measurements possible, each of the two termination designs denoted by the prefix "E-" and "F-" on the figure, will be mounted in three different waveguide structures, for a total of six chips in a single block. First in the ALMA standard, denoted on figure 5.1 with suffix "-760", secondly in each of the WR2.2 and then in the WR3.4 sizes, using a built-in 2.5mm long linear-taper size transitions between

the standard sizes to the 760 μm wide size the terminations were designed for.

With the ALMA Bands 6-7 being the frequency range of 210-370 GHz, the waveguide size chosen for it falls in between the ranges of standard waveguides such as are found in the VNA frequency extenders used for the measurements [39, 40]. Waveguide names, dimensions, and the frequency range of the VNA extenders is listed in table 5.1.

Waveguide standard	**Width** [μm]	**Height** [μm]	**Frequency range [GHz]**
ALMA Band 6-7	760	380	210 - 370
WR2.2	559	279	330 - 500
WR3.4	864	432	220 - 330

Table 5.1: Waveguide sizes and dimensions, and frequency range of the Virginia Diodes VNA extenders used for measuring the WR sizes

The waveguide blocks were milled in-house, out of solid block of aluminum alloy, using a precision CNC.

5.2 E-probe

The first step towards the lithographic process is to make the photomasks which control the layers and locations of the to-be-deposited metals, one layer for Au and another layer for TiN. Alignment between layers is critical, so alignment marks are on both layers, and made in a way so they line up but the first doesn't block the second. Since the width and length of the substrate is another important factor, the size of each chip is delimited at the corners with marks to guide the dicing process.

Also included on the mask are thin-film resistors of different L/w aspect ratios of TiN resistive thin-film, to verify the sheet resistance by measuring their resistance, shown in figure 6.3. The dimensions selected were, as indicated on the mask, $L/W = [3, 5, 8]$, and for a sheet resistance of 30 $\Omega/\square$ should correspond to resistance values of 90, 150 and 240 Ω, following the theory outlined in 3.1. The test structures also include contact pads of Au, and the length is measured as only the length of TiN between them. The thickness of TiN deposition by sputtering, and so its sheet resistance, may vary slightly with radius from the center, so structures are located at different radii.

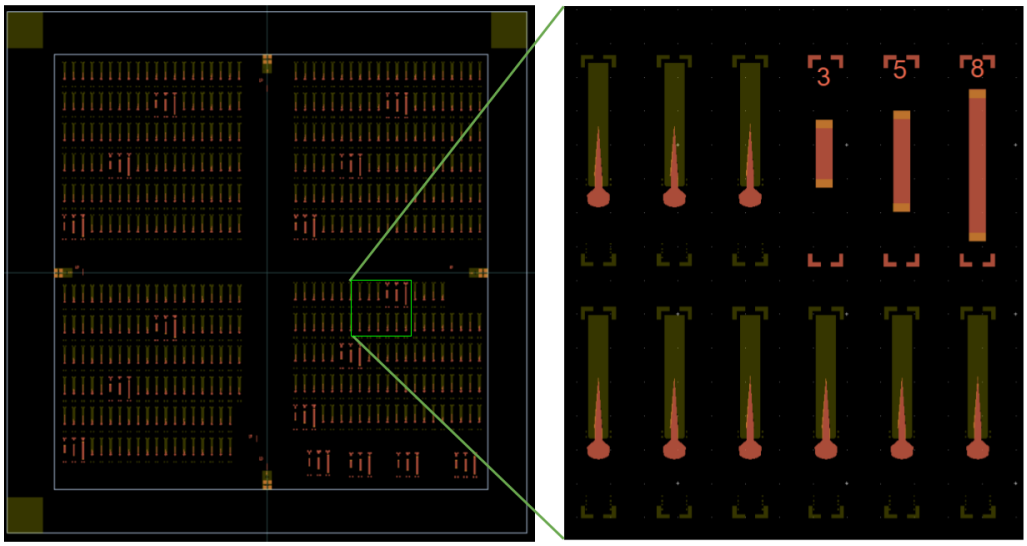

Figure 5.2: Layout of mask on 1x1" quartz, the inset picture showing a higher magnification of several copies of the E-probe, and three sheet resistance test strips to measure the sheet resistance of the thin-film

The fabrication process is described in Fig. 5.3. For simplicity, cleaning steps are mostly left out, and the 10 nm titanium adhesion layer between Au and quartz is only described in the text.

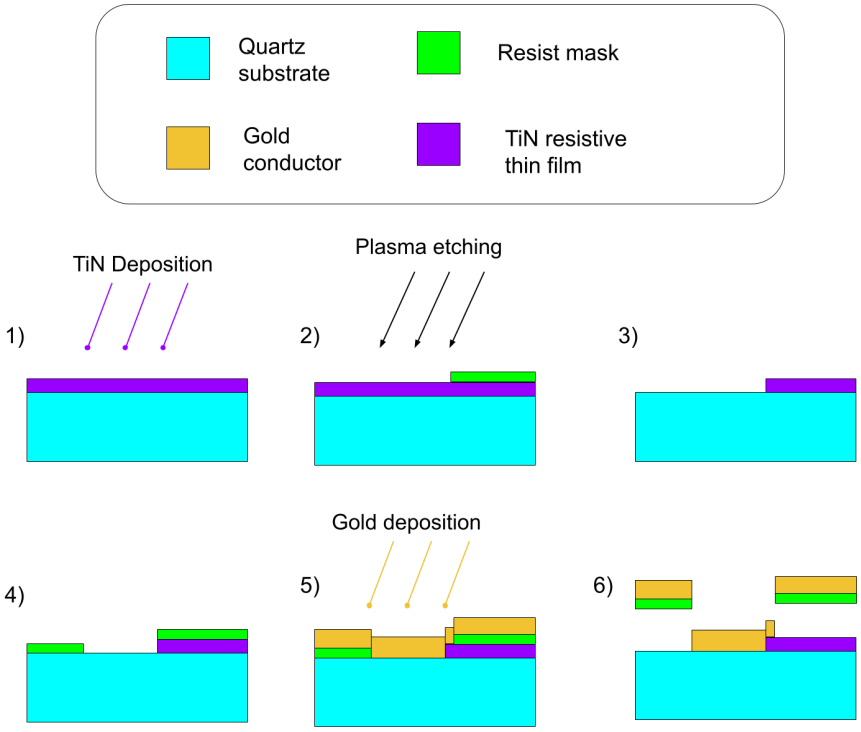

Figure 5.3: Graphic showing the deposition steps and layers of the lithography, and etching process for the E-probe design. Layer thicknesses only indicative, not to scale.

The steps to fabricate the E-probe based design are as follows, leaving out washing and cleaning as needed between stages:

1. Sputter TiN over the whole quartz chip. Measure sheet resistance at this point, to verify correct TiN process. Sheet resistance may increase by 2-4% over the course of a few days due to oxidization.
2. First layer of the photomask, for the TiN layer. This layer is positive-mask, which means that it exposes the areas where sputtered TiN should be removed, leaving only the areas where TiN should remain, covered with resist after development.
3. This leaves the resistive microstrip termination, ready for the next stage.
4. Apply resist with mask. The second mask exposes the areas where Au should remain, so those areas get covered by resist. The mask covers the areas where Au should no remain.
5. Electron beam evaporation of Au on quartz substrate. First step is a 10 nm thick layer of titanium, to improve adhesion between Au and quartz. Electron-beam evaporated gold, to 500 nm thickness.
6. Wash in organic solvent and ultrasonic cleaner, which dissolves the polymer resist mask, releasing the gold from where it should not remain. Rinse off solvent with distilled water, and clean with pressurized air.

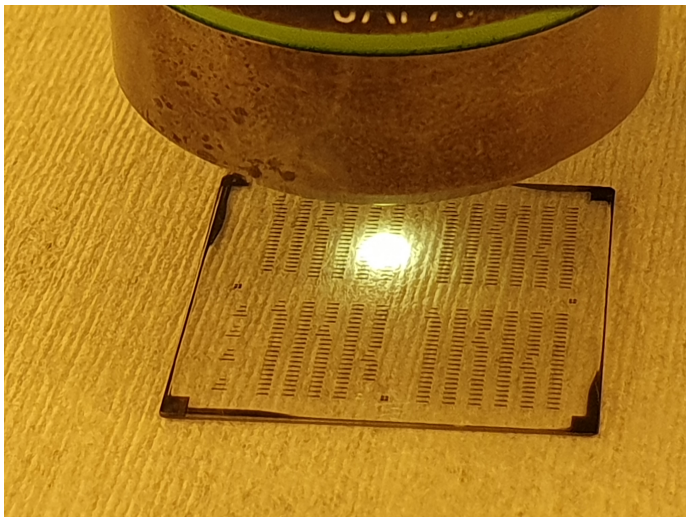

Figure 5.4: Inspection of quartz substrate with E-probe based design under microscope, after TiN sputtering, step 3)

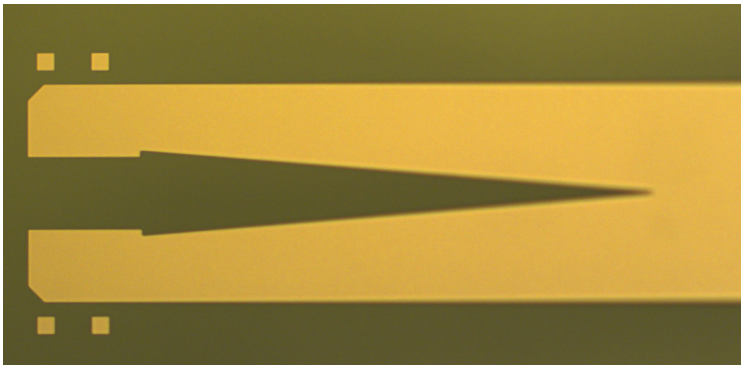

Figure 5.5: Microscope photo of TiN layer, after step 3) in the process.

After the lithography, the chip is ready for dicing. The dicing marks are a part of the TiN layer. It is diced by a very fine 50 μm thick diamond circular sawblade. After dicing, the chips are ready to be released from the glass backing structure, cleaned more, and mounted in the waveguide block.

5.2.1 Mounting in waveguide

To align the E-probe correctly in the substrate channel, alignment marks made of 5x5 μm TiN squares placed on opposite sides of the edges between the substrate channel and the input waveguide. To facilitate mounting and alignment in the substrate channel, a second cavity on the far-side of the probe was added, far left on the pictures. It has the same height above substrate, but extends 10 μm below it, deliberately a short distance so that the edge can be made very sharp and straight, to assist with alignment. Space around the substrate on that also helps getting tools near it to place and align it, but has negligible effect on the electromagnetic behaviour, as was confirmed in simulations.

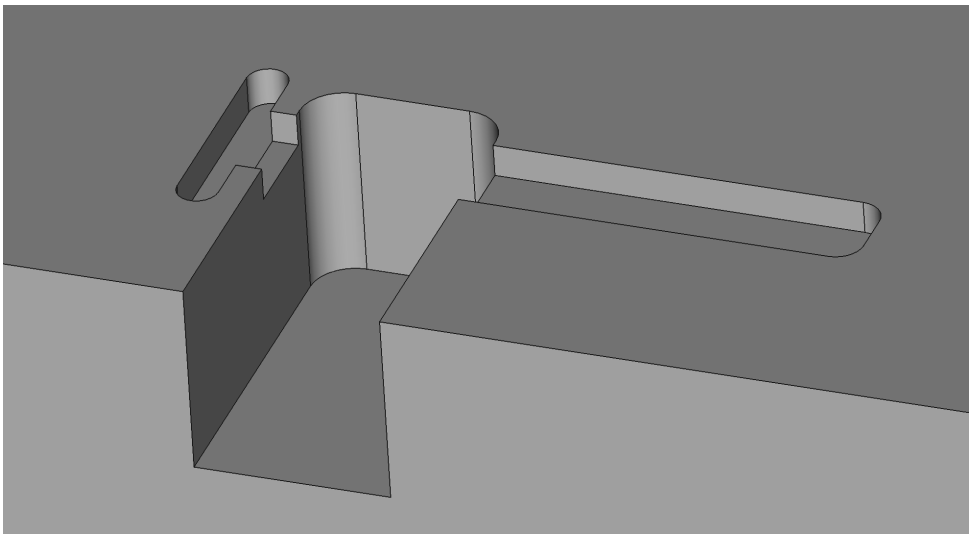

Figure 5.6: Part of the lower half of the splitblock waveguide model, showing the substrate channel and alignment cavity

The mounting is performed under a microscope, and after an adequate position is achieved, the substrate is fixed in place using a thin layer of wax applied under heating. The wax is convenient for prototyping since it is possible to re-heat it to loosen it if the position is not good enough, and it is easy to clean off if that's needed. For a more permanent fixing and production, UV-cured glue will be the used. When the E-probe based waveguide termination has been aligned and fixed, it is ready for measurement.

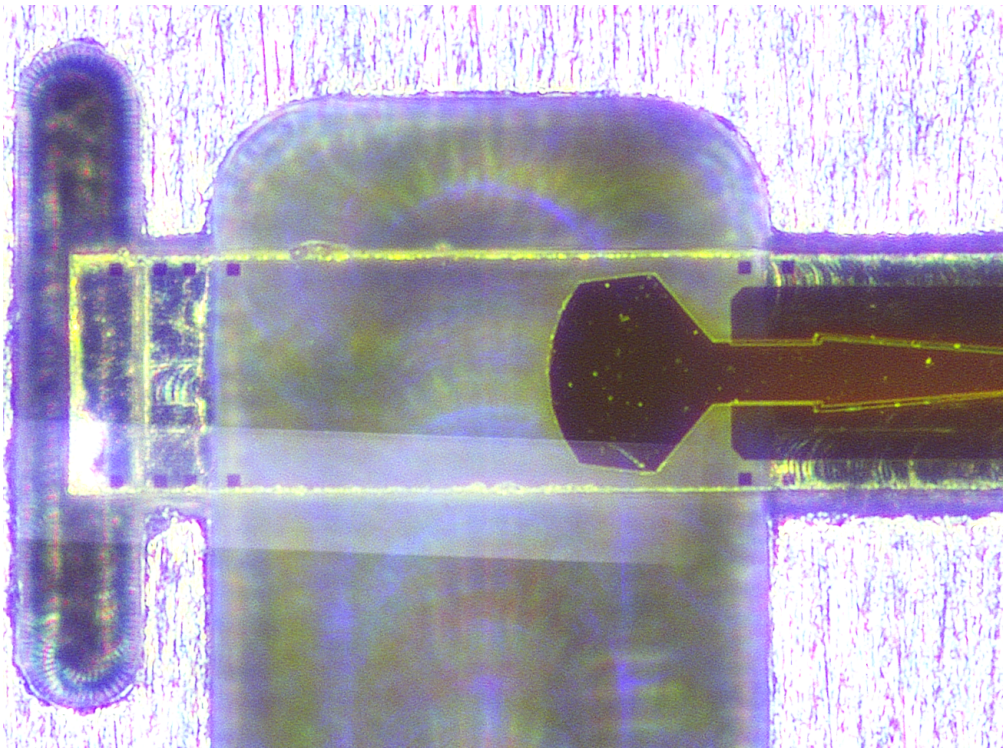

Figure 5.7: Focus-stacked microscope picture of the mounted E-probe waveguide termination

Fig. 5.7 above compares the view of the E-probe based waveguide termination as it appears in a microscope versus how it appears in the computer model as in Fig. 5.8, and highlights the challenge of mounting and aligning chips manually at such size scales.

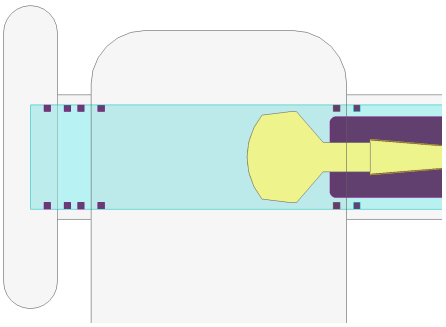

Figure 5.8: 3d model from the same angle as the microscope picture

5.3 Finline

The photomask for the finline structure fabrication is a single layer, only defining the shape of the finline with the mounting-tab. This removes the step of manually aligning the two or more masks during fabrication. Similar resistive strip test structures as on the quartz, for measuring sheet resistance, were included on this wafer as well.

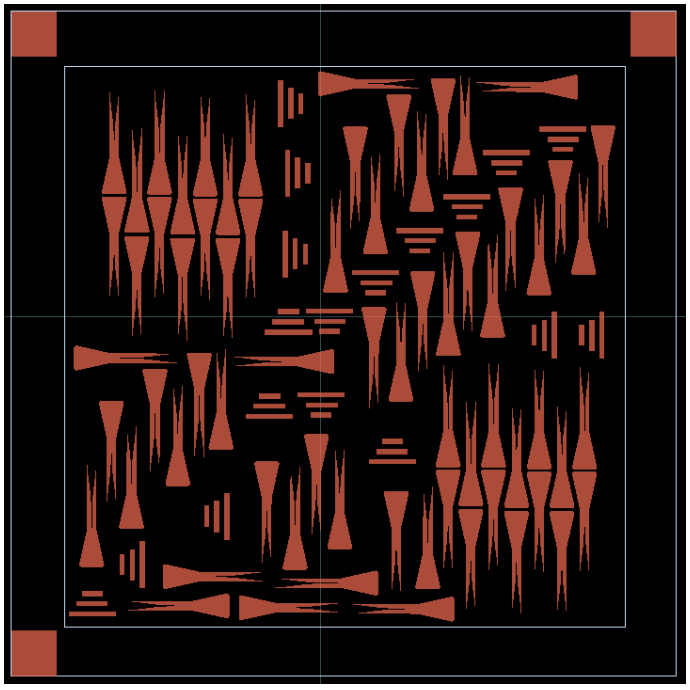

Figure 5.9: Mask layout for finline on 1x1" silicon wafer, showing several copies to be fabricated, along with alignment marks and resistance test strips.

The materials used for the finline are a 30 μm thick high-resistivity silicon as a substrate. From the manufacturer it comes mounted on a 300 μm thick silicon, and but separated from the other one by a 2 μm thick layer of SiOx insulator. TiN is then used as the resistive material.

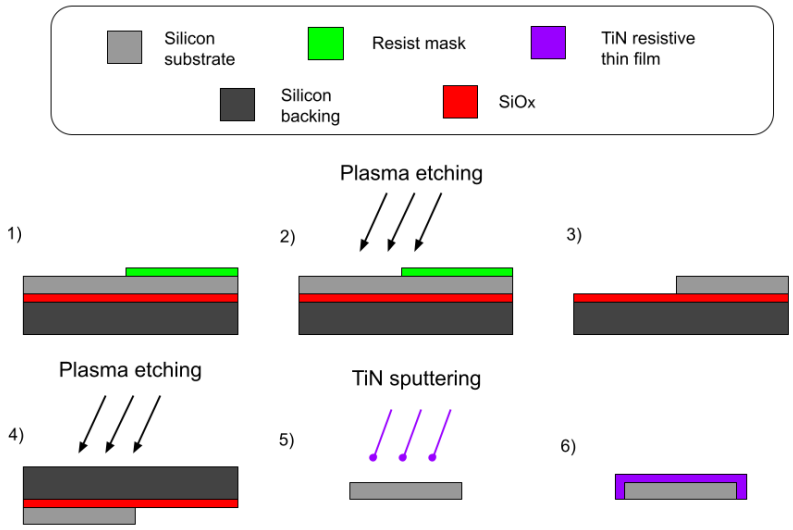

Figure 5.10: Graphic showing steps of the etching and lithography process for the Finline design. Layer thicknesses only indicative, not to scale.

The fabrication process for the finline structure, as described in Fig. 5.10, only consists of shaping the structure using silicon micro-machining, i.e. by etching away with plasma, a process that can be highly anisotropic. The remaining structure is then covered with resistive thin-film. Omitting some cleaning steps for the sake of brevity, the process is as follows:

1. Using the mask, deposit etch-resist on top of the silicon substrate where the shape should remain, to protect it from the plasma etching.
2. Etch by plasma, to a depth of 30 μm, using the buried SiOx layer as an etch-stop.
3. This leaves the finline structure sticking out on top of the SiOx insulator and silicon backing structure.
4. Turning the wafer around, etch away the 300 μm thick backing structure and SiOx insulator, to release the individual finline chips.
5. Sputter TiN over the loose and individual chips to the target sheet resistance of 30 $\Omega/\square$.
6. The TiN covers the finline chips on top, and on the sides.

After the TiN has been sputtered over the Finline chips, they are ready to be mounted in the waveguide block.

5.3.1 Mounting in waveguide

Due to the elongated and narrow shape of the finline, and since it floats in the waveguide without touching any walls, it was decided to make it longer and wider to the back, to move its center of gravity so that it could be more easily placed in the splitblock waveguide.The triangular back-tab also gives a larger and less brittle area to hold and manipulate the miniature piece during installation. The triangle also has the added effect of making the chip easy to align, or effectively self-aligning.

The effects of the back-tab on the electromagnetic behaviour are negligible, but the height of the air-space above its TiN-coated side matters, shown on figure 5.13, as it still carries some currents. Using a slightly more involved fabrication, it might be worth exploring to omit the TiN on most of the back-tab, and only sputter the original shape as shown on figure 4.22, and leave the backtap as only silicon substrate.

Figure 5.11: Finline structure with triangular back-tab to facilitate mounting and maneuvering

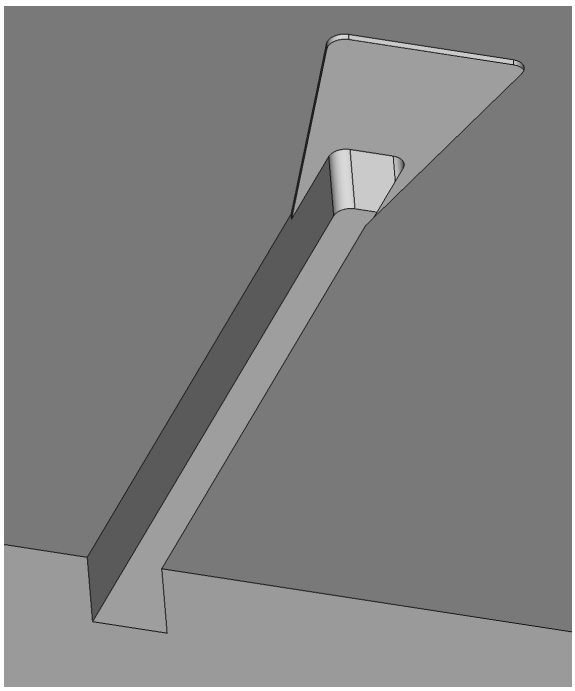

Figure 5.12: Lower half of splitblock waveguide for finline structure, showing the slot in which the back-tab sits

As previously mentioned, the thickness of the finline substrate is 30 μm, and the depth of the slot in the lower half of the splitblock is the same, so when mounted it should sit flush with the block surface. The upper half of split-block in turn has 40 μm of space above it. Since there is still some electric field propagating in this part of the finline structure, the height of the space above the finline is important, and using simulations this height was found to give the best performance. The triangular back-tab has a 10 μm space to all sides, both to account for CNC milling tolerances and to to make mounting easier.

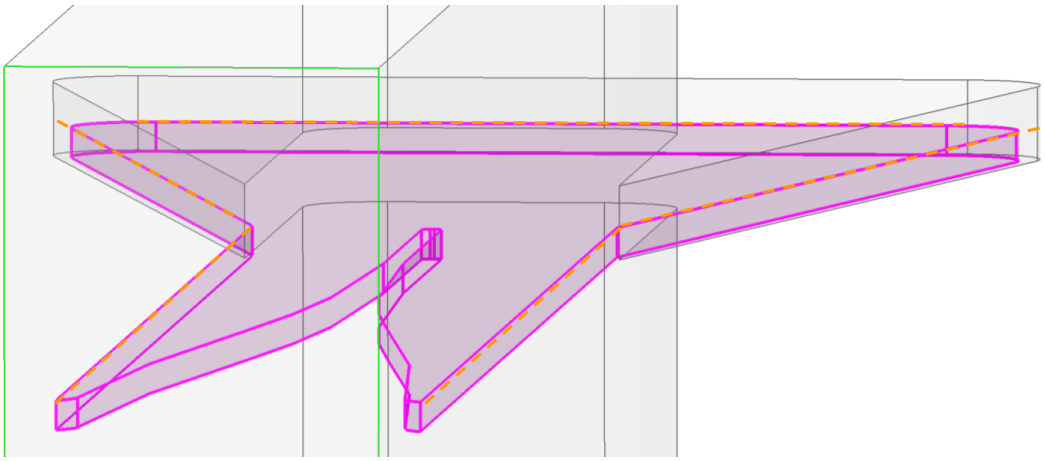

Figure 5.13: Figure showing the finline structure, outlined in pink, mounted in the waveguide, emphasizing the space around the backtab. The finline structure sits on a solid shelf, with some air space above and around it. The split plane is indicated with dashed lines.

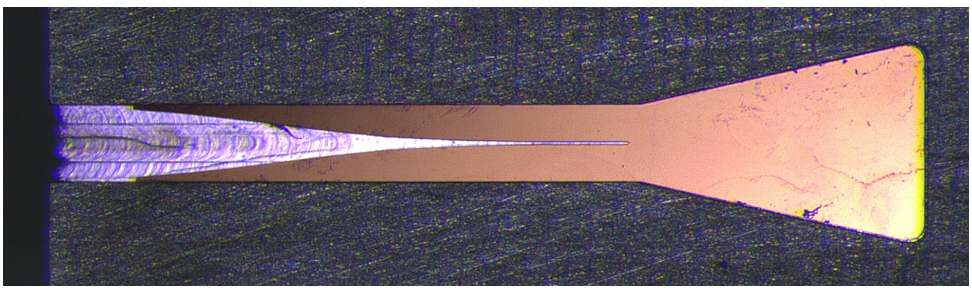

Figure 5.14: Microscope picture showing the finline mounted in the waveguide.

It is noteworthy on figure 5.14 how the reflection of light from the surface of the mounted finline shows a gradient to shadow towards the left. This was inspected in a 3D microscope and found to correspond to a slight tilt, the tips flexed upwards, 10 μm higher at the tips than in the backtab. This could cause mechanical stress or slightly degraded performance, and was fixed after the picture was made.

With the very tips of the finline structure being 30 μm wide, from the substrate thickness, and only to 10 μm thick, there is a risk that tips may break during processing, such as in the cleaning process following the micro-fabrication, which utilizes ultrasonic vibration in a bath of organic solvents to clean the resist layers. This may prompt some reconsideration of the design towards slightly wider tips.

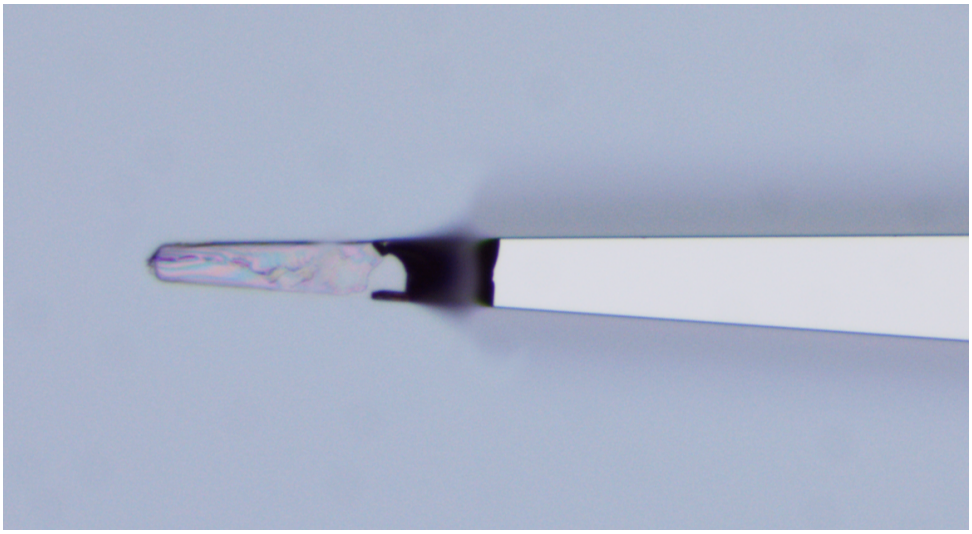

Figure 5.15: Focus-stacked microscope picture showing a broken tip of one finline structure

A few chips of the finline design broke in the fabrication, like shown on Fig. 5.15, and the faults were only visible through a microscope, so the whole silicon wafer required careful checking. Many samples however were in good shape, were chosen to proceed to the sputtering stage after visual verification.

6

Measurement and characterization

This chapter deals with the measurements and measurement results of the two waveguide terminations.

Section 6.1 describes measurements of sheet resistance of the fabricated TiN resistive thin-film, using the test strip resistors.

Section 6.2 shows the VNA measurement setup, and includes a discussion on the uncertainties most relevant to this project involved in terahertz measurements in section 6.2.1, and the measurement of these components in particular in sections 6.2.2 for the E-probe and 6.2.3 for the finline, finishing with some concluding words about the measurements.

Each waveguide termination design has three chips in the waveguide block, one at its intended waveguide size of 760x380 μm, and at each of the WR standard sizes which will be used for measurement. This is outlined in detail in table 5.1 and shown in Fig. 5.1. In the measurement discussion they will be simply referred to with "E-" and "F-" prefixes for the E-probe and Finline, and "-760" or "-WR" suffixes for the different waveguide size ports, for shorthand. I.e. F-760, F-WR3.4, or F-WR for the whole measured band using both WR waveguides.

6.1 Measuring the thin-film resistance

The TiN resistive thin-film is a key element in this design, serving the purpose of dissipating the RF energy with conductor or ohmic losses. The target sheet resistance in the design and fabrication process was 30 $\Omega/\square$. Test structures were included on the chips to enable measurements of the sheet resistance, for process quality control. The test structures consist of strips of the resistive thin films, fabricated in L/w or length/width aspect ratios of 3, 5 and 8, which should result in values of 90, 150 and 240 Ω for the resistive film test strips. Their ends are covered with gold contact pads, which are deposited on top of part of the TiN. But the designed resistance value is based on only the length of TiN not covered by gold, i.e. the pure TiN between the gold pads. The measurement system is expected to have some internal resistances, so having several measurement points makes it possible to calculate and compensate for it. The test strips were measured by the voltage/current relationship as current passes through the structures.

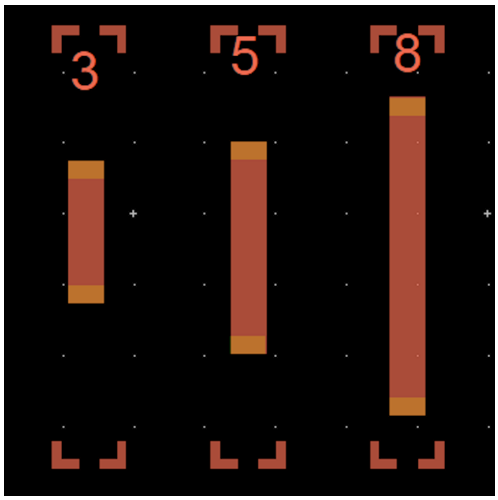

Figure 6.1: Resistive strips on mask, identified by their L/w proportions. Gold pads visible on the ends of each

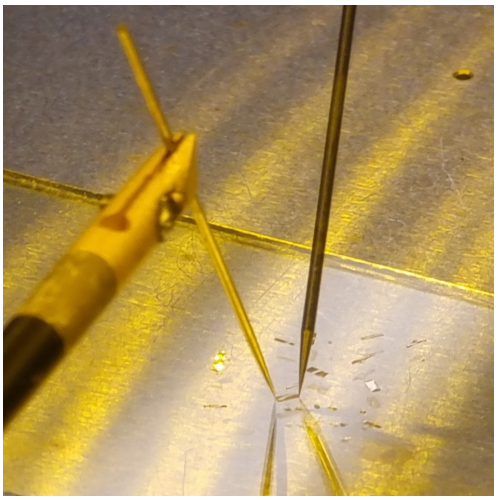

Figure 6.2: Resistance measurement setup of test strips

Fine-tipped tungsten needles are placed on the gold contact pads by using a microscope and micromanipulators, to establish electrical contact on the microscopic resistive test strips, to perform the resistance measurement.

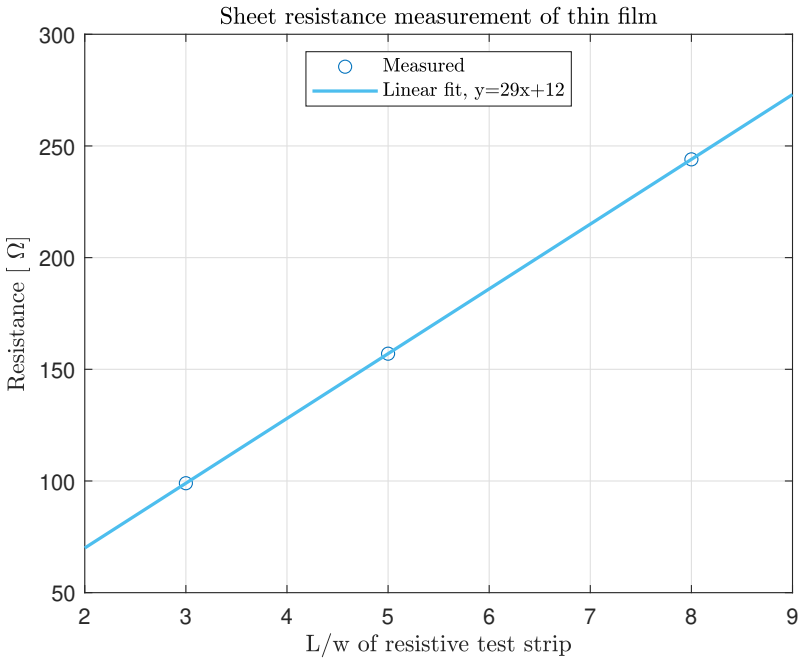

Figure 6.3: Resistance measurement results of resistive thin-film test strips on quartz

The three different strips give three different resistance values, each of which includes the systems internal resistances connected in series. The slope of the line between them indicates the sheet resistance, and the Y-offset indicates the resis-

tances in the measurement setup, i.e. probe contact resistance, probe resistance and probe-lead resistance. The sheet resistance was calculated to be 29 $\Omega/\square$, to a high degree of accuracy, with series resistance of 12 Ω, i.e. contact resistance and lead resistance. Using this method of several measuring points enables us to separate the measured values and the built-in errors of the measuring system.

6.2 VNA measurements

The Vector Network Analyzer (VNA) is the fundamental tool used to measure and characterize microwave components and systems. It is possibly the most precise electronic instrument used for those purposes [20]. It can measure across a broad dynamic range of power and frequency, and with a high frequency resolution. Not less importantly, the measurement results can be traceable to calibration standards and physical dimensions. An important part of this excellent precision is that error corrections, sometimes called calibrations, are an inherent part of its use. Almost any discrepancies in its performance, such as deviation from flatness of frequency response or non-ideal behaviour of its internal RF couplers, can be characterized by relatively simple user-performed routines before measurements and their effects removed mathematically by the VNA itself.

In certain measurement setups the effects of connectors or cables can be effectively removed as well, or their impact on measurement results made negligible. To achieve some degree of repeatability, many screw connectors such as the SMA and their higher frequency variants like the 1mm connector, should be connected only using manufactured provided torque wrenches so that each connector mating cycle connects to a similar level of torque. Some other effects are however very hard or practically impossible to remove. This includes effects such as from the misalignment of waveguide flanges during mounting, or especially waveguide shims, or other operations where exact repeatability is difficult to achieve, and is an ongoing topic of research in THz metrology [41] and has been studied by several authors, such as [42] and [43], and in the case of ALMA specifically it has led to publications of specific recommendations for the design standards of waveguide flanges, see [44] and [45].

The VNA used for these measurements was a Keysight PNA-X Network Analyzer, with a native frequency range of 10 MHz-26.5 GHz. To reach the frequency range required, the VNA's functionality is extended with Virginia Diodes Frequency extenders, in waveguide sized and frequency capabilities WR2.2 for 325-500 GHz and WR3.4 for 200-330 GHz respectively. They were calibrated in the beginning of each measuring session using through-reflect-match (TRM) calibration with the supplied calibration kit, and the calibration drift assessed at the end of each session.

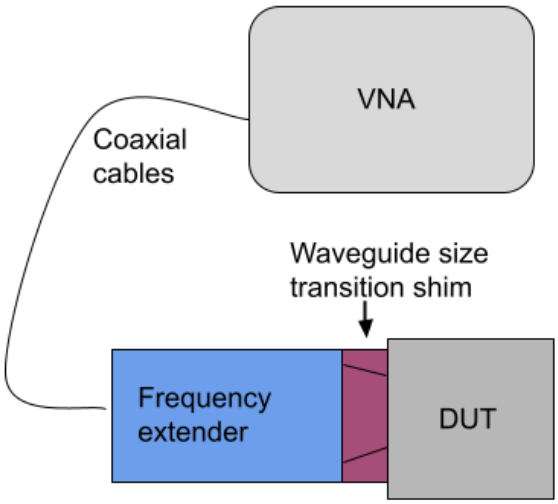

Figure 6.4: VNA setup. The size transition shim is used for measuring the 760x380 sized waveguides, but is not needed nor used for the standard WR waveguide ports

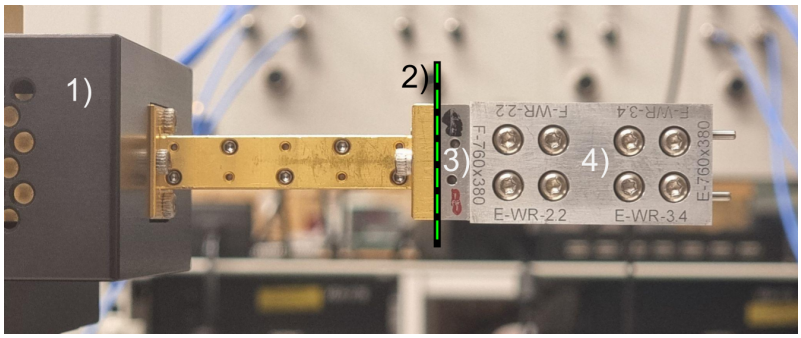

Figure 6.5: Photograph showing part of VNA setup: frequency extender (1), the calibration plane (2) marked with green dashed line, waveguide size transition shim (3) and the waveguide block containing the DUT (4). Measuring Finline 760x380 port

De-embedding, or error correcting for test fixtures, is a mathematical method applied during post-processing of VNA measurement data. Its aim is generally to remove the unwanted effects of structures around the device-under-test (DUT) so that the measurement results more closely show the performance of the DUT itself, with less influence from i.e. the test setup or waveguide losses. In the case demonstrated here, the goal is first to correct errors from conductor losses which happen in the waveguide structure itself. As outlined in section 3.1, conductor loss increases at higher frequencies, for longer waveguides it can be significant and at cryogenic temperatures it increases even more for normal conductors. The second goal is to examine the effects of the waveguide flanges.

S-parameters serve well to describe the behaviour of microwave circuits and components, in terms of ratios of incident and scattered waves at each port. The drawback of S-parameters is that the S-matrices can not be cascaded using matrix algebra, since more complicated relationships apply. The solution to this is to transform them to T-matrices, which account for this and can be both cascaded and manipulated in standard matrix algebra. In that way we can describe the measured S-matrix as the cascade of the DUT's T-matrix and the T-matrices of the test fixture.

$$[T_{measured}] = [T_A][T_{DUT}][T_B] \tag{6.1}$$

Since the T matrices are invertible and cascadable, we can simply deembed the DUT's T-matrix, by using matrix algebra:

$$[T_{DUT}] = [T_A]^{-1}[T_{measured}][T_B]^{-1} \tag{6.2}$$

And from there transform the $[T_{DUT}]$ back into and S-matrix. But to do that, a S-matrix or a T-matrix of the fixture or transitions needs to be constructed, and its constituent values must be repeatable between different measurements.

6.2.1 Exploration of sources of error in VNA measurement

Several sources of error are characterized by the VNA through the calibration process, and are automatically removed from subsequent measurements. This is possible with sources of error that are predictable and more or less repeatable, especially if they arise on the VNA side of the calibration plane. One type of error we can compensate for here is conductor loss in the waveguide itself, shown in figure 6.2.1.1.

But when it comes to connecting different waveguide parts together with their flanges, a random error is introduced, which is not repeatable and can not be calibrated away with standard error correction methods. It is at least possible to get an impression of its scale relative to the measured value, as detailed in section 6.2.1.2.

6.2.1.1 Waveguide losses

As outlined in section 3.1, metal conductivity decreases with increased frequency. And although waveguides are among the better transport media for high frequency RF, they still suffer from this to some extent. The waveguide terminations are by their nature measured inside a waveguide, and in that case waveguide losses are in fact favorable for their function, but it is of interest to see to which extent the measured performance is due to the termination itself and what the contribution of waveguide losses really is.

Two ways to evaluate the waveguide losses were explored: First, the reflection from the waveguides for the terminations were measured without any terminations, as they are pictured in figures 5.6 and 5.12. Since this is a one-port measurement already calibrated against a reflect standard or waveguide short, any deviation from $S_{11} = 0$ corresponds to energy dissipated in the walls of the waveguide. At this level of reflections, the waveguide flange mismatch discussed in section 6.2.1.2 is relatively insignificant, but certainly also involved.

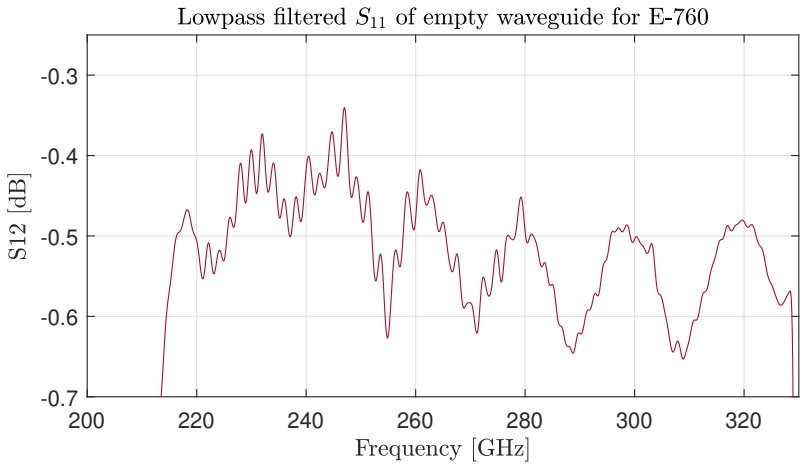

Figure 6.6: Measured S_{11} from empty waveguide block, through one waveguide size transition, for E-760. Lowpass filtered for clarity of demonstration

As is seen on the plot, the contribution only by in the waveguide are on the order of -0.4 dB to -0.5 dB. Note that this particular waveguide was especially short, 700 μm and includes a 5.5 mm transition, for a total of 6.2 mm one way distance from the calibration plane. This conductor loss means for example that if a given termination measured at -25 dB, -24.5 dB would be from the termination itself, but -0.5 dB from the waveguide containing it. This level of waveguide loss can be taken to be close to consistent between measurements, easy to compensate for and in this case has little significance. At cryogenic temperatures, this would be expected to increase and almost double, with increased resistivity of normal conductors.

Using the T-matrices described in section 3.3.3, and following a method outlined in [46], where we model the reflection as being forwarded through the cascaded T-matrices rather than reflected back, we can set this up as:

$$\begin{bmatrix} \rho & 0 \\ 0 & 0 \end{bmatrix} \begin{bmatrix} e^{-j\pi} & 0 \\ 0 & 0 \end{bmatrix} \begin{bmatrix} \rho & 0 \\ 0 & 0 \end{bmatrix} = \begin{bmatrix} \rho_m & 0 \\ 0 & 0 \end{bmatrix} \tag{6.3}$$

Where ρ is the one-way loss, the $e^{-j\pi}$ is the wave reflection of an ideal short, and ρ_m is what is measured and shown on plot 6.9. Keeping in mind that $T_{11} = S_{21}^{-1}$ makes this more intuitive.

Then we get the T-matrix of the DUT, which can be easily converted to an S-matrix to deembed the loss.

$$[T_{DUT}] = [T_A]^{-1}[T_{measured}][T_B]^{-1} \tag{6.4}$$

6.2.1.2 Waveguide flange misalignment

At the level of reflections these terminations aim to achieve, misaligned waveguide flanges turn out to be a significant contribution to the reflected power measured at the VNA. To get an impression of the scale of their impact, we set up a measurement of two transitions back-to-back, or a 2xThru, as shown in diagram 6.7. This introduces three waveguide flanges with potential misalignment, but terminated on both sides by VNA ports. Each time this is connected and disconnected, a different misalignment is made, in three places.

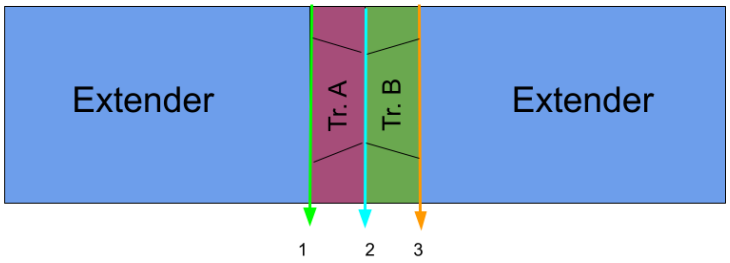

Figure 6.7: VNA setup of 2xThru measurement. Locations of waveguide flanges with potential for misalignment marked in numbers, 1-3,

Viewing the same setup from inside the waveguide, from right to left, what we might see is something like what is shown in figure 6.8. Note that this is an exaggerated view. But with waveguide dimensions on the scale of 760x380 μm a mismatch of even as little as 30 μm e.g. in the up-down or E-field direction is near 8% of the physical dimension. A misalignment of 30 μm is more than is expected from a careful measurement setup, but is presented here as an example.

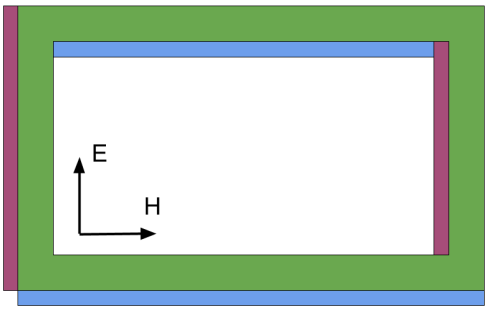

Figure 6.8: A cross-section view of exaggerated waveguide flange misalignment, as seen through the waveguide, showing the axis of the electric field and magnetic field, for a TE_{10} mode

Assuming only a TE_{10} mode propagating, a discontinuity in the E-plane (blue box) on Fig. 6.8, presents a capacitance to the incoming wave. A discontinuity in the H-plane (red box), presents inductance. These added imaginary parts to

the impedance reduce the quality of the matching and limit the power transfer, as outlined in the theory on power transfer in section 3.9. What power is not delivered forward or dissipated in the waveguide walls is reflected back and adds to the measured Γ.

Measuring the S_{11} parameter in this 2xThru setup, over both WR frequency bands demonstrates in one plot, Fig. 6.9, both how strong the reflection off the misaligned flanges can be, and how it can vary between setups, i.e. the one for WR3.4 and WR2.2.

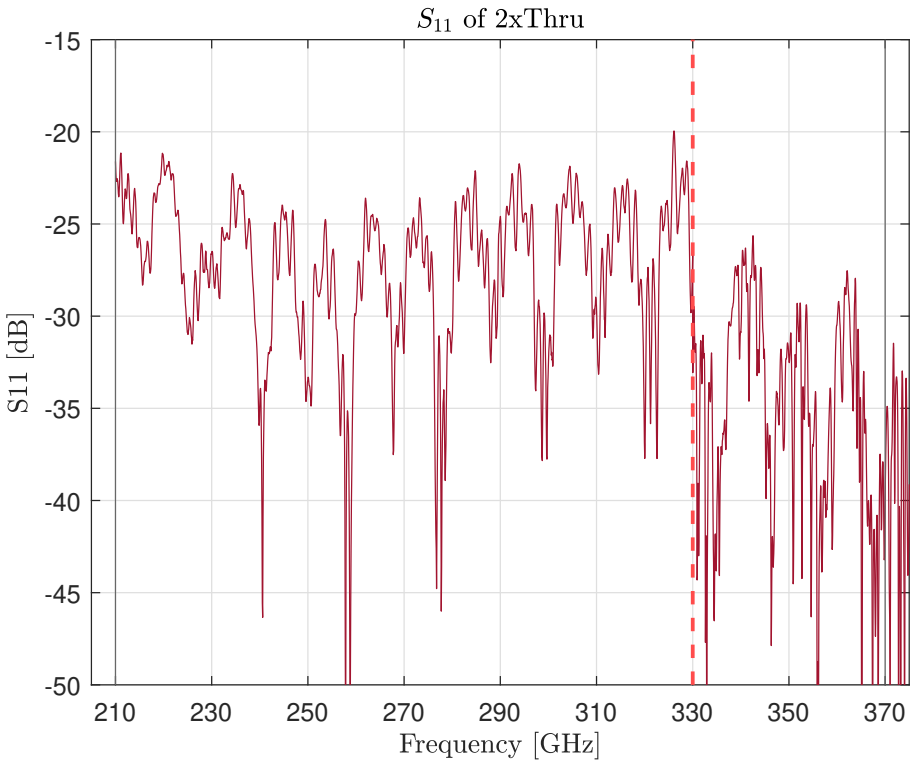

Figure 6.9: Measured S_{11} of the 2xThru setup, with potential for 3 misaligned waveguide flanges. The red dashed line shows where the WR3.4 and WR2.2 are joined

Plot 6.9 shows that in the lower waveguide band the reflections from the transitions are on the order of -22 to -24 dB, and in the higher band they improve by several dB. This could be due to better calibration, or it might be factors like better transition shims, or by chance by less misalignment. This effect is high in this measurement since there are a total of 3 waveguide flanges being joined, for purposes of demonstration. In the measurements on the 760x380 waveguide size there is one transition, so there are two flanges being joined, shown on Fig. 6.11, and in the native WR sizes there is only one, at the calibration plane, between the VNA and the waveguide block containing the DUT.

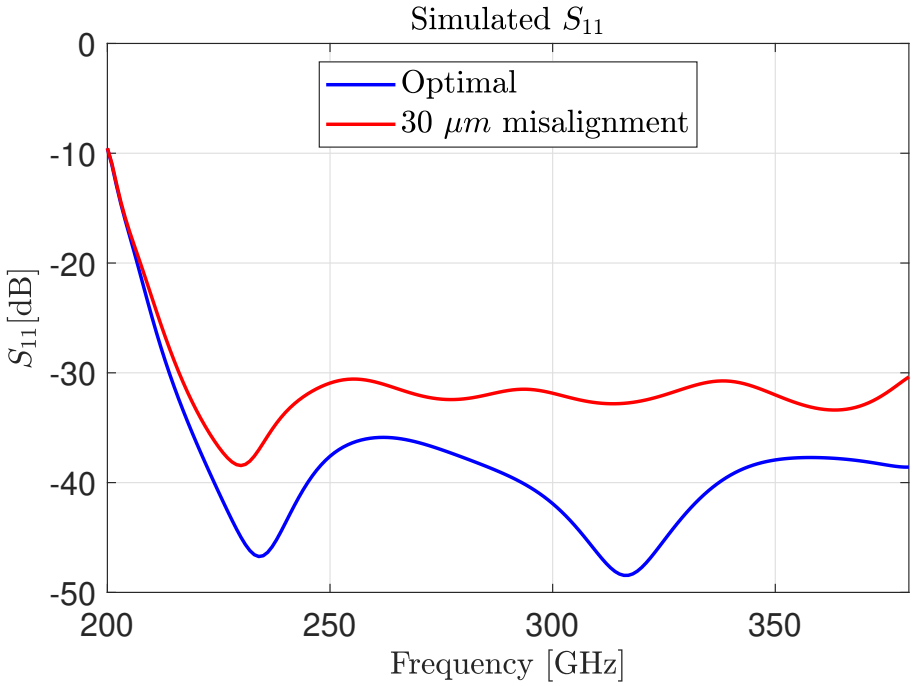

Figure 6.10: Simulated S_{11} comparison of the finline termination, with a single 30 μm E-plane misalignment (red) v.s. perfect alignment (blue)

The reason for this is the following. If we model the reflection coefficient which is measured at the VNA's calibration plane, it can be described by the following sum of terms, assuming that the power in multiple reflections are negligible (i.e. the VNA port at least is well impedance matched) [47].

$$\Gamma_{measured} = S_{11,fl} + \frac{S_{21,fl}\, S_{12,fl}\, \Gamma_{load}}{1 - S_{11,fl}\, \Gamma_{load}} \tag{6.5}$$

Where $S_{11,fl}$ is the reflection off one flange, $S_{21,fl}$ and $S_{12,fl}$ are the insertion loss of an an intermediary waveguide shim, such as an size transition, and Γ_{load} is the actual (but unknown) reflection coefficient of the termination. It is seen that if $S_{11,fl}$ is on the same order of magnitude as the Γ_{load}, given a reasonable $S_{21,fl}S_{12,fl}$, then it heavily affects the $\Gamma_{measured}$. The order of magnitude of this effect can be estimated by setting up a 2xThru measurement of the waveguide size transitions, as shown in Fig. 6.7 and measurement results in Fig. 6.9, and even more by performing 3D full-wave EM simulations of the mismatch, like is shown in Fig. 6.10. But as it is likely to vary randomly between each instance, deembedding its estimated effects is not scientifically valid and will not be done.

The effect is a combination of reflections that are not separable in frequency-domain, but with high enough resolution they may be separable in the time-domain. Since the waves are scattered off surfaces at different distances from the VNA port, they arrive back at the VNA at different times, but on a timescale of picoseconds. Using a longer waveguide to house the termination, so its reflections arrive even later, this effect could be enhanced and thus made more separable by temporal analysis.

6.2.2 VNA measurements of E-probe waveguide termination

Following is the measurement data of the E-probe based waveguide termination. Referring back to the layout of probes on the waveguide block, the different E-probes will be referred to as E-760 in the 760x380 waveguide, measured through transitions, and E-WR in the WR standard sizes. The DUT is measured using two separate waveguide bands, but they are conjoined in the plots, and the joining is marked with a red dashed line.

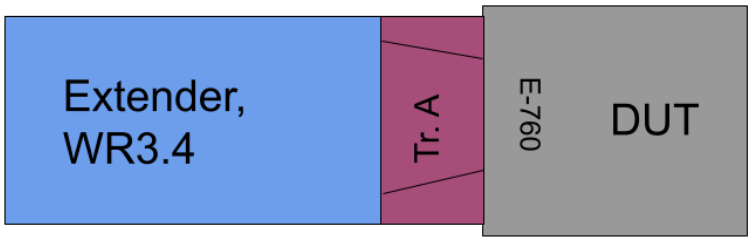

Figure 6.11: Example of a VNA setup, showing WR3.4 extender, and a waveguide size transition A down to 760 μm waveguide containing the E-probe termination. Same transitions are used for E-760 and F-760

Fig. 6.11 shows an example of how the 760x380 waveguide ports are measured, using a 5.5 mm long waveguide size transitions. Both the E-760 and the F-760 are measured in this way.

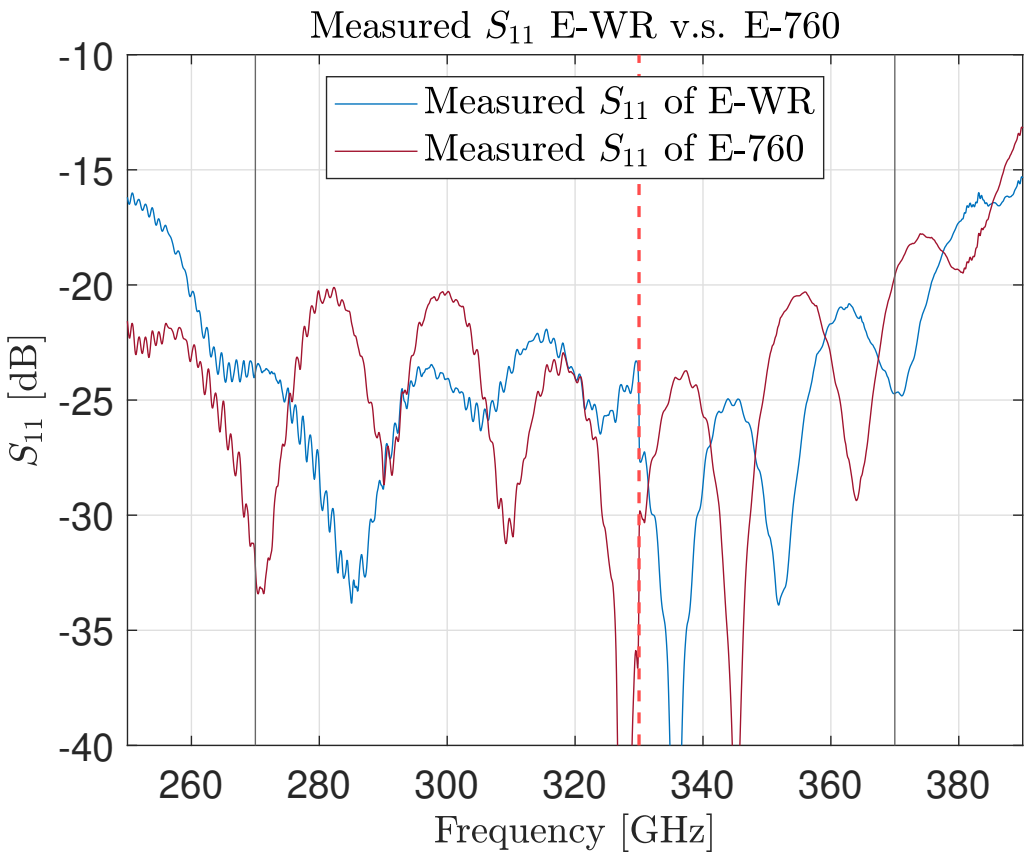

Figure 6.12: Measured S_{11}, compared between E-WR and E-760

The measurements of the E-WR3.4 and E-WR2.2 terminations are markedly better than the E-760, showing clearly that built-in waveguide size transitions are much better, adding only one flange to the measurement instead of the size transition shims that add two. But with the alignment sensitivity of the E-probe, described in section 4.1.8, it is hard to evaluate how much of this is due to misalignments of the probe-and-substrate, or misalignments of the waveguide transition on E-760. Comparing the better measurement result, of the E-WR, to the ideal, simulated performance, we see the following plot:

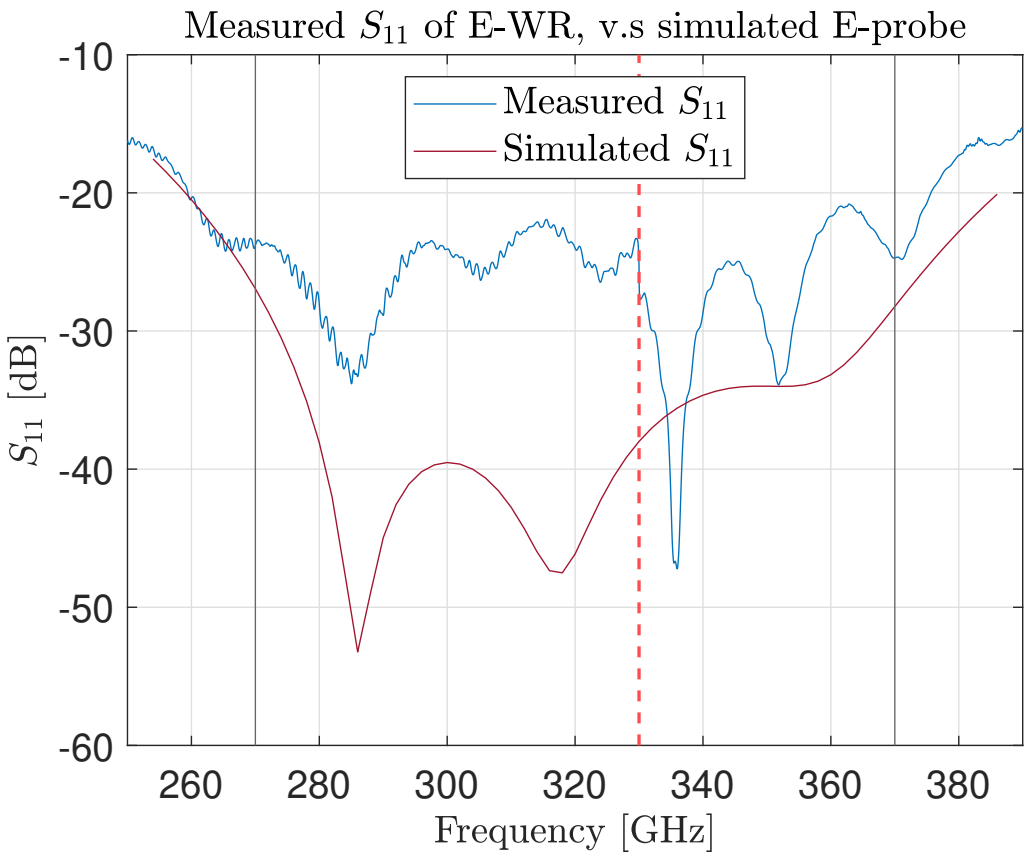

Figure 6.13: Comparison between the simulated S_{11} of the E-probe design, and the measured E-WR

The overall performance shown here on Fig. 6.13 is significantly lacking from coming close to the simulations, being closer to -23 dB over most of the band, than the -26 dB at the edges and significantly lower in the center which the simulations showed. The difference between WR3.4 and WR2.2 is noteworthy however, seen on the lower and upper side respectively of the red dashed line at 330 GHz.

6.2.3 VNA measurements of Finline waveguide termination

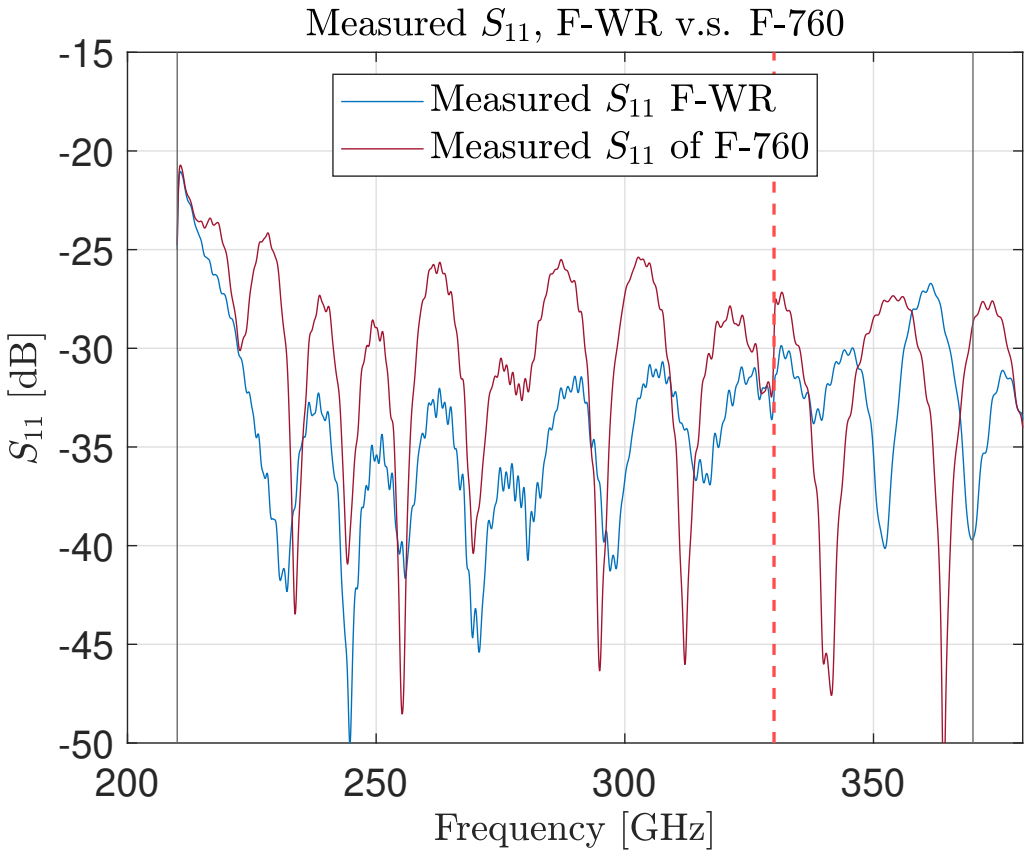

Figure 6.14: Measured S_{11} of F-WR v.s. F-760

The F-760 with the waveguide size transition shims is again showing worse performance, with clear reflections across the whole band, and a measured performance barely under -26 dB. From comparisons with the F-WR and the prior discussion in section 6.2.1.2, it is tempting to make assumptions about some of those reflections origination in misaligned waveguide flange, but that conclusion waits more irrefutable evidence to isolate that as the main cause.

Like with the E-probe based termination, the better performing is the one natively in the waveguide sizes of the VNA frequency extenders, the F-WR. Comparing that now with the simulated ideal performance, and the simulated 30 μm waveguide flange misalignment,

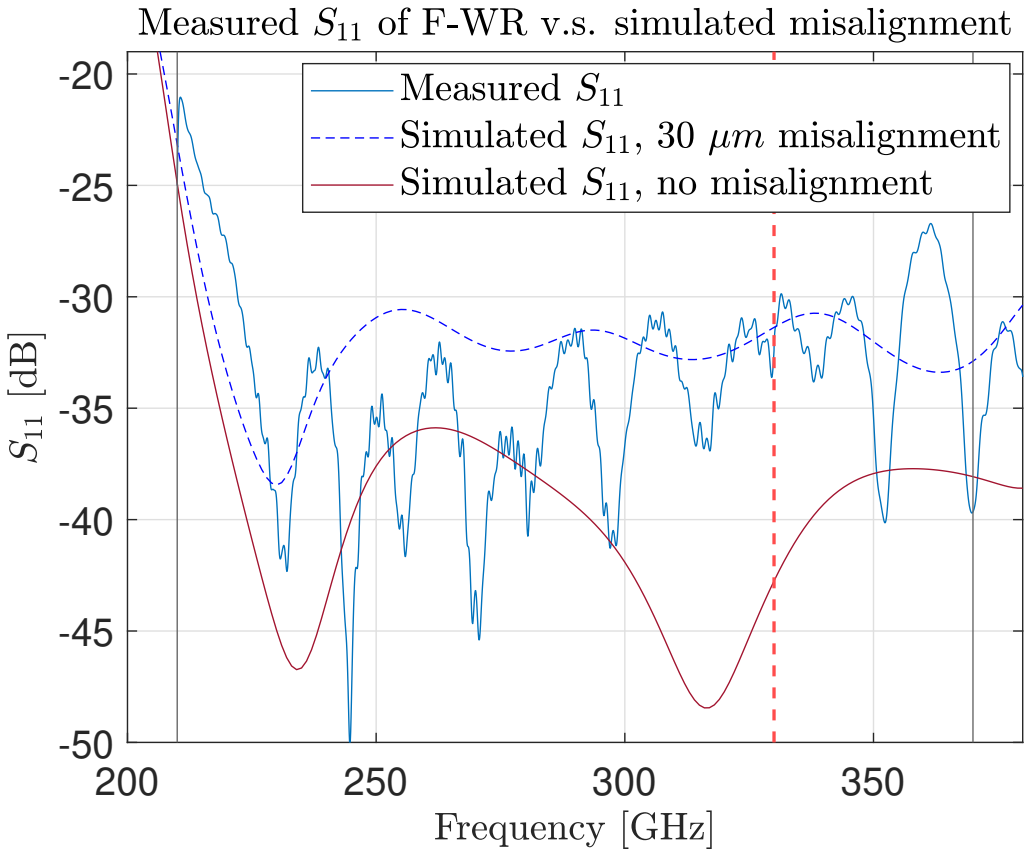

Figure 6.15: Simulated S11 comparison of the finline termination, with a single 30 μm E-plane misalignment v.s. simulated perfect alignment

Figure 6.15 shows a comparison between the measured F-WR finline, the ideal simulated one, and a simulation that includes a single 30 μm misalignment of a waveguide. We see here that the scale of the measured reflections reaches close to the significantly reduced performance of the simulated 30 μm misalignment, but also shows slightly different behaviour in some places. On the lower frequency end, the level of reflection only reaches -30 dB around 250 GHz, rather than the approximately 220 GHz of the ideal termination. This could indicate a misalignment in the H-plane, which could both increase the cut-off frequency f_c of the TE_{10} mode higher by making it more narrow, as described by formula 3.21, and introduce an inductive waveguide step.

6.3 Measurement conclusion

We see from these measurements, theory and simulations, that each waveguide flange adds significant reflections. From three flanges in the 2xThru measurements giving reflections on the order of -25 dB, to two flanges in the measurements on the E-760 and F-760 terminations, and then measurements with one flange on the terminations natively in WR waveguide sizes, improving the measured performance of the finline by up to 6 dB.

From these measurements it is clear that the Finline-based waveguide termination shows excellent performance. Whether it comes close to its simulated performance of -37.5 dB, or is limited to -30 dB, is hard to draw decisive conclusions about, given the unpredictability of the errors involved. But from the discussion about sources of errors 6.2.1 and the measurements and simulations that estimate the presence and scale of errors, it is possible to conclude that the is possibly better than the measurements show.

The intended use and placement of this termination is in a 2SB receiver topology, where the termination is integrated into the waveguide mixer block and not attached with waveguide flanges. Additionally, this system will be used at cryogenic temperatures, where the conductivity of the waveguide walls will be limited even further by the anomalous skin effect. While generally a detriment to the function of radioastronomy equipment, in this case it improves the performance in practice.

7
Conclusion

Two waveguide terminations were designed, fabricated and measured. The different designs were based on two distinct principles, one using an E-field probe or E-probe to couple the RF energy from waveguide into microstrip on quartz substrate, and dissipate it in a lossy conductor. The other using a tapered finline structure directly in the waveguide itself. Both showed excellent performance in simulations, demonstrating that either one is a viable method for this task, at least in the ideal world of 3D full-wave simulators.

The goal was to achieve a waveguide termination that would cover the whole waveguide band of 210-370 GHz, with the lowest achievable reflection coefficient, using simple and well established clean room and micro-fabrication fabrication methods, and materials that have predictable and reliable performance at cryogenic temperatures. This succeeded entirely in the case of the Finline, and to a lesser extent in the case of the E-probe.

The measured performance of the E-probe termination was significantly lower than shown in simulations, only achieving near -23 dB across its bandwidth of 270-370 GHz, and the design suffered from impractically low tolerance to mounting misalignment. It has been shown that the E-probe based design is a fully viable method of terminating a waveguide. But this particular E-probe only shows excellent performance in ideal simulations of perfect alignment, which poses inconvenient problems in the real world of errors and inaccuracies. Another E-probe design, more tolerant to mounting position errors, might serve this goal better. Towards that goal, a useful and simple approach to designing rectangular, resistive microstrip terminations has been worked out and described.

The Finline termination achieved -37.5 dB from 220-390 in simulations, and at least -30 dB in measurements, and it is concluded that limitations to the measurement method likely underestimate its performance. Additionally it was simple to fabricate and mount in the waveguide, is reasonably robust mechanically, and as finlines are known to be, not very sensitive to alignment issues. To boot, it is possible to fabricate it in a self-aligning way, such as was done here with the triangular backtab. Aside from this particular mounting-tab implementation, the active part of it is 2.5mm long, so if there is not a strict limit on space, it is a very effective and convenient waveguide termination, which, if implemented, may improve the performance of future 2SB SIS radioastronomy receivers.

Bibliography

[1] Christopher K. Walker. *Terahertz Astronomy*. CRC Press, 2016.

[2] information@eso.org. *ALMA vision*. en. URL: https://www.eso.org/public/images/esopia00080illus/ (visited on 05/09/2023).

[3] F. P. Mena et al. "Design and Performance of a 600–720-GHz Sideband-Separating Receiver Using \hboxAlO_x and AlN SIS Junctions". In: *IEEE Transactions on Microwave Theory and Techniques* 59.1 (Jan. 2011). Conference Name: IEEE Transactions on Microwave Theory and Techniques, pp. 166–177. ISSN: 1557-9670. DOI: 10.1109/TMTT.2010.2090417.

[4] V. Belitsky et al. "SEPIA - a new single pixel receiver at the APEX Telescope". In: *Astronomy & Astrophysics* 612 (Apr. 2018). arXiv:1712.07396 [astro-ph], A23. ISSN: 0004-6361, 1432-0746. DOI: 10.1051/0004-6361/201731458. URL: http://arxiv.org/abs/1712.07396 (visited on 01/25/2023).

[5] Bhushan Billade et al. "Performance of the First ALMA Band 5 Production Cartridge". In: *IEEE Transactions on Terahertz Science and Technology* 2.2 (Mar. 2012). Conference Name: IEEE Transactions on Terahertz Science and Technology, pp. 208–214. ISSN: 2156-3446. DOI: 10.1109/TTHZ.2011.2182220.

[6] Andrey Khudchenko et al. "Efficiency of the Image Band Suppression in Sideband Separating SIS Receivers for Radio Astronomy". In: *2020 7th All-Russian Microwave Conference (RMC)*. Nov. 2020, pp. 19–20. DOI: 10.1109/RMC50626.2020.9312246.

[7] Ronald Hesper et al. "A Sideband-Separating Mixer Upgrade for ALMA Band 9". en. In: (2009).

[8] *Eccosorb Microwave Absorbers*. en. URL: https://www.eccosorb.eu/Eccosorb.html (visited on 05/05/2023).

[9] G.A. Ediss et al. "FTS measurements of eccosorb MF112 at room temperature and 5 K from 300 GHz to 2.4 GHz". In: *Alma memos* 273 (Sept. 1999).

[10] H. Hemmati, J.C. Mather, and W.H. Eichhorn. "Submillimeter and millimeter wave characteriation of absorbing materials". In: *Applied Optics* 24.24 (Dec. 1985), pp. 4489–4492.

[11] F.P. Mena and A.M. Baryshev. "Design and simulation of waveguide load for ALMA-band 9". In: *Alma memos* 513 (). URL: https://science.nrao.edu/facilities/alma/aboutALMA/Technology/ALMA_Memo_Series/alma513/memo513.pdf.

[12] A.R. Kerr and et. al. “MF-112 and MF-116: Compact waveguide loads and FTS measurements at room temperature and 5 K.” In: *Alma memos* 494 (). URL: https://library.nrao.edu/public/memos/alma/main/memo494.pdf.

[13] Bernhard Beuerle, Umer Shah, and Joachim Oberhammer. “Micromachined Waveguides with Integrated Silicon Absorbers and Attenuators at 220–325 GHz”. In: *2018 IEEE/MTT-S International Microwave Symposium - IMS*. ISSN: 2576-7216. June 2018, pp. 579–582. DOI: 10.1109/MWSYM.2018.8439364.

[14] R.R. Monje et al. “High quality microstrip termination for MMIC and millimeter-wave applications”. In: *IEEE MTT-S International Microwave Symposium Digest, 2005.* ISSN: 0149-645X. June 2005, pp. 1827–1830. DOI: 10.1109/MWSYM.2005.1517082.

[15] Ahmed Gouda et al. “Millimeter-Wave Wideband Waveguide Power Divider With Improved Isolation Between Output Ports”. In: *IEEE Transactions on Terahertz Science and Technology* 11.4 (July 2021). Conference Name: IEEE Transactions on Terahertz Science and Technology, pp. 408–416. ISSN: 2156-3446. DOI: 10.1109/TTHZ.2021.3078876.

[16] Dimitris Pavlidis, ed. *Fundamentals of Terahertz devices and applications*. 2021.

[17] David M. Pozar. *Microwave Engineering*. 4th ed. Wiley, 2011.

[18] Ramesh Garg, Inder Bahl, and Maurizio Bozzi. *Microstrip Lines and Slotlines*. 3rd. Artech House, 2013.

[19] Jia-Sheng Hong. *Microstrip Filters for RF/Microwave Applications*. 2nd. Wiley, 2011.

[20] Joel P. Dunsmore. *Handbook of Microwave Component Measurements width Advanced VNA Techniques*. Wiley, 2012.

[21] R. G. Chambers. “The Anomalous Skin Effect”. In: *Proceedings of the Royal Society of London. Series A, Mathematical and Physical Sciences* 215.1123 (1952). Publisher: The Royal Society, pp. 481–497. ISSN: 0080-4630. URL: https://www.jstor.org/stable/99095 (visited on 06/01/2023).

[22] E. Maxwell. “Conductivity of Metallic Surfaces at Microwave Frequencies”. en. In: *Journal of Applied Physics* 18.7 (July 1947), pp. 629–638. ISSN: 0021-8979, 1089-7550. DOI: 10.1063/1.1697818. URL: https://pubs.aip.org/aip/jap/article/18/7/629-638/158884 (visited on 06/07/2023).

[23] R. Finger and A. R. Kerr. “Microwave Loss Reduction in Cryogenically Cooled Conductors”. en. In: *International Journal of Infrared and Millimeter Waves* 29.10 (Oct. 2008), pp. 924–932. ISSN: 0195-9271, 1572-9559. DOI: 10.1007/s10762-008-9394-1. URL: http://link.springer.com/10.1007/s10762-008-9394-1 (visited on 06/07/2023).

[24] "The surface impedance of superconductors and normal metals at high frequencies II. The anomalous skin effect in normal metals". en. In: *Proceedings of the Royal Society of London. Series A. Mathematical and Physical Sciences* 191.1026 (Nov. 1947), pp. 385–399. ISSN: 0080-4630, 2053-9169. DOI: 10.1098/rspa.1947.0122. URL: https://royalsocietypublishing.org/doi/10.1098/rspa.1947.0122 (visited on 06/07/2023).

[25] A. Mellberg et al. "Fabrication and Characterization of Reactively Sputtered TaN Thin-Film Resistors for Millimeter Wave Applications". en. In: *Electrochemical and Solid-State Letters* 7.11 (Oct. 2004). Publisher: IOP Publishing, G261. ISSN: 1944-8775. DOI: 10.1149/1.1804985. URL: https://iopscience.iop.org/article/10.1149/1.1804985/meta (visited on 05/08/2023).

[26] Anna Malmros et al. "TiN thin film resistors for monolithic microwave integrated circuits". en. In: *Journal of Vacuum Science & Technology B, Nanotechnology and Microelectronics: Materials, Processing, Measurement, and Phenomena* 28.5 (Sept. 2010), pp. 912–915. ISSN: 2166-2746, 2166-2754. DOI: 10.1116/1.3475532. URL: https://pubs.aip.org/avs/jvb/article/28/5/912-915/468283 (visited on 05/08/2023).

[27] Z. Wang, J. Deen, and A. Rahal. "Accurate Modelling of Thin-Film Resistor up to 40 GHz". In: *32nd European Solid-State Device Research Conference*. Sept. 2002, pp. 307–310. DOI: 10.1109/ESSDERC.2002.194930.

[28] S. Horst et al. "Modeling and characterization of thin film broadband resistors on LCP for RF applications". In: *56th Electronic Components and Technology Conference 2006*. ISSN: 2377-5726. May 2006, 5 pp.–-. DOI: 10.1109/ECTC.2006.1645895.

[29] P.J. Meier. "Two New Integrated-Circuit Media with Special Advantages at Millimeter Wavelengths". In: *1972 IEEE GMTT International Microwave Symposium*. May 1972, pp. 221–223. DOI: 10.1109/GMTT.1972.1123053.

[30] P.J. Meier. "Integrated Fin-Line Millimeter Components". In: *IEEE Transactions on Microwave Theory and Techniques* 22.12 (Dec. 1974). Conference Name: IEEE Transactions on Microwave Theory and Techniques, pp. 1209–1216. ISSN: 1557-9670. DOI: 10.1109/TMTT.1974.1128465.

[31] Maria Rosa M. L. Albuquerque et al. "Accurate Design of Finline Tapers for Millimeter Wave Applications". en. In: *International Journal of Infrared and Millimeter Waves* 26.6 (June 2005), pp. 855–866. ISSN: 1572-9559. DOI: 10.1007/s10762-005-5658-1. URL: https://doi.org/10.1007/s10762-005-5658-1 (visited on 05/03/2023).

[32] Cristian López et al. "Waveguide-to-Substrate Transition Based on Unilateral Substrateless Finline Structure: Design, Fabrication, and Characterization". In: *IEEE Transactions on Terahertz Science and Technology* 10.6 (Nov. 2020), pp. 668–676. ISSN: 2156-3446. DOI: 10.1109/TTHZ.2020.3020683.

[33] P. Meyer and C.A.W. Vale. “Designing high-performance finline tapers with vector-based optimization”. In: *1999 IEEE MTT-S International Microwave Symposium Digest (Cat. No.99CH36282)*. Vol. 2. June 1999, 707–710 vol.2. DOI: 10.1109/MWSYM.1999.779858.

[34] J. W. Kooi and et. al. “A full-height waveguide to thin-film microstrip transition with exceptional RF bandiwidth and coupling efficiency”. In: *International journal of infrared and Millimeter waves* 24.3 (Mar. 2003).

[35] Johanna Hanning et al. “A broadband THz waveguide-to-suspended stripline loop-probe transition”. In: *2017 IEEE MTT-S International Microwave Symposium (IMS)*. June 2017, pp. 1091–1094. DOI: 10.1109/MWSYM.2017.8058785.

[36] Jungsik Kim, Wonseok Choe, and Jinho Jeong. “Submillimeter-Wave Waveguide-to-Microstrip Transitions for Wide Circuits/Wafers”. In: *IEEE Transactions on Terahertz Science and Technology* 7.4 (July 2017). Conference Name: IEEE Transactions on Terahertz Science and Technology, pp. 440–445. ISSN: 2156-3446. DOI: 10.1109/TTHZ.2017.2701151.

[37] Chunguang Ma et al. “Broadband Waveguid-to-CPWG Transition With Butterfly-shaped Dipole”. In: *2021 46th International Conference on Infrared, Millimeter and Terahertz Waves (IRMMW-THz)*. ISSN: 2162-2035. Aug. 2021, pp. 1–2. DOI: 10.1109/IRMMW-THz50926.2021.9567018.

[38] Min Wan et al. *Characterization of silicon in the terahertz*. Mar. 2020. DOI: 10.1117/12.2547339.

[39] *WR3.4VNAX*. URL: https://vadiodes.com/en/wr3-4vnax (visited on 06/09/2023).

[40] *WR2.2VNAX*. URL: https://vadiodes.com/en/wr2-2vnax (visited on 06/09/2023).

[41] Dylan F. Williams. “500 GHz–750 GHz Rectangular-Waveguide Vector-Network-Analyzer Calibrations”. In: *IEEE Transactions on Terahertz Science and Technology* 1.2 (Nov. 2011). Conference Name: IEEE Transactions on Terahertz Science and Technology, pp. 364–377. ISSN: 2156-3446. DOI: 10.1109/TTHZ.2011.2127370.

[42] Charles Oleson and Anthony Denning. “Millimeter Wave Vector Analysis Calibration and Measurement Problems Caused by Common Waveguide Irregularities”. In: *56th ARFTG Conference Digest*. Vol. 38. Nov. 2000, pp. 1–9. DOI: 10.1109/ARFTG.2000.327428.

[43] Andy Fung et al. “Two-Port Vector Network Analyzer Measurements Up to 508 GHz”. In: *IEEE Transactions on Instrumentation and Measurement* 57.6 (June 2008). Conference Name: IEEE Transactions on Instrumentation and Measurement, pp. 1166–1170. ISSN: 1557-9662. DOI: 10.1109/TIM.2007.915125.

[44] A R Kerr, E Wollack, and N Horner. “Waveguide Flanges for ALMA Instrumentation”. en. In: 278 (1999).

[45] ALMA Memo. “Recommendations for Flat and Anti-Cocking Waveguide Flanges”. en. In: ().

[46] Hawal Marouf Rashid. “Towards Ultimate Performance of THz Heterodyne Receivers: SIS Frequency Multiplier and Wideband Passive Components”. en. ISBN: 9789175973722. PhD thesis. Chalmers University of Technology, 2016. URL: https://research.chalmers.se/en/publication/235281 (visited on 06/07/2023).

[47] *2.8: Return Loss, Substitution Loss, and Insertion Loss*. en. Oct. 2020. URL: https://eng.libretexts.org/Bookshelves/Electrical_Engineering/Electronics/Microwave_and_RF_Design_III_-_Networks_(Steer)/02%3A_Chapter_2/2.8%3A_Return_Loss_Substitution_Loss_and_Insertion_Loss (visited on 06/07/2023).

DEPARTMENT OF SPACE, EARTH AND THE ENVIRONMENT
CHALMERS UNIVERSITY OF TECHNOLOGY
Gothenburg, Sweden
www.chalmers.se

CHALMERS
UNIVERSITY OF TECHNOLOGY